Received: 31 July 2023 | Revised: 25 September 2023 | Accepted: 26 September 2023

DOI: 10.1002/hsr2.1622

ORIGINAL RESEARCH

Health Science Reports Open Access WILEY

Pyroptosis-related gene signatures are associated with prognosis and tumor microenvironment infiltration in head and neck cancer

Yan Long[1] | Yadong Wu[2] | Juxiang Peng[3] | Jukun Song[2] | Na Li[4]

[1]Department of Medical Cosmetology, Guizhou Provincial People's Hospital, Guiyang, Guizhou, China

[2]Department of Oral and Maxillofacial Surgery, The Affiliated Stomatological Hospital of Guizhou Medical University, Guiyang, China

[3]Department of Orthodontics, Guiyang Stomatological Hospital, Guiyang, Guizhou, China

[4]The Obstetrics and Gynecology Department, The Second Affiliated Hospital of Zunyi Medical University, Zunyi, China

Correspondence

Jukun Song, Department of Oral and Maxillofacial Surgery, the Affiliated Stomatological Hospital of Guizhou Medical University, Guiyang, China.
Email: songjukun@163.com

Na Li, The Obstetrics and Gynecology Department of the Second Affiliated Hospital of Zunyi Medical University, Zunyi, China.
Email: foxlina2008@163.com

Funding information

Guizhou Provincial People's Hospital Youth Fund, Grant/Award Number: GZSYQN [2016]09

Abstract

Background and Aims: Recent studies have highlighted the biological significance of pyroptosis in cancer development. Nevertheless, it is still uncertain if pyroptosis also plays a part in immune modulation and the creation of the tumor microenvironment (TME).

Methods: The pyroptosis regulatory genes (PRGs) were comprehensively assessed in 1938 head and neck cancer samples, and systematically correlated these modification patterns with the infiltration characteristics of TME cells. The unsupervised consensus analysis method was used to identify specific pyroptosis clusters. The single-sample gene set enrichment analysis and CIBERSOFT algorithms were used to evaluate the infiltration levels of various immune cell subsets. A principal component analysis algorithm was used to construct the pyrolysis potential index (PPI) to quantify the pyrolysis regulation patterns in head and neck squamous cell carcinoma (HNSC).

Results: Pyrophosphate regulatory genes (PRGs) are often upregulated in tumors due to mutations. PRGs relate to various clinical outcomes and pathways. Molecular subtyping identified pyroptosis patterns, which align with three tumor immunophenotypes: immune-inflamed, immune-excluded, and immune-desert. The PPI measures pyrolysis roles, showing higher PPI in tumor samples linked to subtypes and clinical characteristics. Lower PPI correlates with longer survival, increased immune activity, more tumor mutations, high PD-L1 expression, and mutations in significant genes like PIK3CA. Such patients also experience enhanced immune responses in immunotherapy trials.

Conclusion: We conducted a comprehensive examination of pyroptosis in HNSC and developed a PPI indicator that shows a strong correlation with the variety and intricacy of the TME.

KEYWORDS

head and neck squamous cell carcinoma, immunotherapy, mutation burden, pyroptosis, tumor microenvironment

1 | INTRODUCTION

Human head and neck squamous cell carcinoma (HNSC) is a prevalent form of cancer, affecting more than 500,000 individuals worldwide annually.[1–3] Even with surgical intervention, radiation treatment, and chemotherapy, approximately 50% of patients succumb to the illness. Stage III/IV tumors are the main subgroup of HNSC.[4] Patients diagnosed with Stage III/IV have a bleak outlook, as indicated by a 40% recurrence-free survival rate and a 60% overall survival (OS) rate over 5 years.[5,6] Hence, there is a requirement for new therapeutic approaches, either through single-drug treatment or a combination of therapies, to enhance the outlook for primary advanced HNSC. Considering the limitations of HNSC treatment, new treatment targets are crucial to improve the clinical efficacy of HNSC. Therefore, there is an urgent need for new reliable prognostic models for more feasible targeted therapies. According to recent research, it has been found that genes associated with pyroptosis (PRGs) are frequently disrupted in cases of head and neck cancer.[7,8] Nevertheless, as far as we know, there has been no systematic analysis conducted on the carcinogenic impacts of PRGs in head and neck cancer.

Regulated cell death, a pathway of programmed cell death, has a significant impact on the development, maintenance of balance, and disease progression in organisms. Pyroptosis, a recently identified form of programmed cell death, is involved in the pathogenesis of several conditions, such as autoimmune disorders, diseases related to immunodeficiency, neurodegenerative disorders, ischemia–reperfusion injuries, and cancer. $CD4^+$ T lymphocytes (immune cells of HIV infection) exhibit resistance to cellular scorching,[9] a process implicated in the development of acute liver injury and acute lung injury.[10,11] Classical cellular scorching of NLRP1 inflammatory vesicles[12] is a significant process that plays a crucial role in the neurodegeneration observed in Alzheimer's disease. With the increasing understanding of pyroptosis, its complex biological function has been uncovered. Drug resistance has also been shown to be linked with pyroptosis and PRGs. According to a previous report by Guo et al.,[13] the regulation of GW4064 was found to trigger pyroptosis in colorectal cancer cells, leading to enhanced chemosensitivity both in vivo and in vitro. In a recent study, it was discovered that BIX-01294 can boost the effectiveness of chemotherapy in gastric cancer through the stimulation of GSDME-mediated pyroptosis.[14] Hence, pyroptosis might have a significant impact on the progression and management of cancer. Exploring the systematic examination of pyroptosis and its disruption in HNSC may prove beneficial for clinical intervention.

Studying the correlation between cell pyroptosis and disease could offer fresh perspectives on the clinical management of the condition. Pyroptosis has been found to have a significant impact on tumor development and antitumor mechanisms, according to the current research. Nevertheless, the examination of its particular role in head and neck cancer remains unexplored. Hence, an organized investigation was carried out to ascertain the levels of expression of PRGs in tissues of head and neck tumors. In addition, the predictive significance and the association between pyroptosis and the immune microenvironment of tumors were investigated. Furthermore, a pyroptotic potential index (PPI) was developed to measure the pyroptosis alteration patterns of individual tumors and forecast the immune therapy response of patients.

2 | MATERIAL AND METHODS

2.1 | Source of data and pre-processing

Seven publicly accessible datasets (GSE27020,[15] GSE31056,[16] GSE30784,[17] GSE39366,[18] GSE41613,[19] GSE65858 [LHNG cohort],[20] and TCGA-HNSC cohort) were utilized to gather messenger RNAs and clinical information. Data of TCGA-HNSC datasets obtained from The Cancer Genome Atlas (TCGA) website were downloaded, specifically RNA sequencing (RNA-seq; fragments per kilobase million value) data. The R package GEOquery.[21] was used to download the microarray data for GSE27020, GSE31056, GSE30784, GSE39366, GSE41613, and GSE65858 from Gene Expression Omnibus (GEO). To remove nonbiological technical biases, the sva package utilized the "ComBat" algorithm.[22] The OS data were available for TCGA-HNSC, GSE27020, GSE31056, GSE41613, and LHNG cohorts. Data on somatic mutation and copy number variation (CNV) were obtained from the TCGA database. To depict the CNV pattern of 33 genes involved in pyroptosis on human chromosomes, the R package "Rcircos" was utilized. The quantification of tumor mutation burden (TMB) involved calculating the number of somatic alterations per megabase within the genome, as stated by Hellmann et al. in 2018.[23]

2.2 | Unsupervised clustering analysis using a consensus algorithm

To identify differentially expressed PRGs, a collection of 33 PRGs was extracted from six integrated GEO datasets. Pyroptosis modification patterns were identified using unsupervised clustering analysis, which was based on the 33 genes regulating pyroptosis. This analysis classified patients into three distinct clusters. To ensure classification stability, the "Pam" method underwent unsupervised clustering analysis using the "ConsensuClusterPlus" R package,[24] which was repeated 1000 times.

2.3 | Functional enrichment analysis and gene set variation analysis

To examine the diversity in biological processes among various pyroptosis modification patterns, we utilized the gene set variation analysis (GSVA)[25] technique with the R package "GSVA." For GSVA analysis, the MSigDB database was used to download the gene sets labeled as "c2.cp.kegg.v6.2.-symbols." The R package "clusterProfiler" was used to perform KEGG annotation for genes relevant to pyroptosis, with a threshold of FDR < 0.05.[26]

2.4 | Assessment of the infiltration of cells in the tumor microenvironment

Quantification of the infiltration levels of various immune cells in HNSC was conducted through a single-sample gene set enrichment analysis (ssGSEA) as described by Barbie et al. in 2009.[27] Recently published studies[27,28] provided gene panels specifically designed for 28 different types of immune cells. The ssGSEA analysis was used to calculate enrichment scores, which represented the relative abundance of tumor microenvironment (TME)-infiltrating cells in each sample.

2.5 | Differential expression analysis between distinct phenotypes

Using the "Limma" R package,[29] differential expression analysis was conducted to identify differentially expressed genes (DEGs) among different subtypes.

2.6 | Principal component analysis dimensionality reduction and establishment of the PPI index

The PPI, known as the pyroptosis gene signature, was developed as a scoring system to assess the pyroptosis patterns in patients with head and neck cancer. To begin with, we chose the shared DEGs obtained from various pyroptosis clusters and employed a univariate Cox regression model to conduct prognostic analysis for each gene. Afterward, principal component analysis (PCA) was employed to extract the first and second principal components as the signature score. In conclusion, a technique resembling prior research[30,31] was utilized to establish the PPI index for every individual.

$$\text{PPI score} = \sum \text{PCiA} + \sum \text{PCiB}.$$

I represent the manifestation of genes related to the m6A phenotype.

2.7 | Somatic alteration data

Data on genetic mutations in patients from the TCGA-HNSC group were obtained from the TCGA site (https//www.cancer.gov/tcga/). The calculation of TMB in HNSC was determined by considering the overall count of non-synonymous mutations. HNSC driver genes were analyzed using the ComplexHeatmap package's "oncoplot" function between high and low immune cell infiltration (ICI) scores.[32] We identified the 25 most frequently altered genes with the highest mutation rate.

2.8 | Prediction of response to chemotherapy/immunotherapy

While immune checkpoint blockade therapies that inhibit T-cell suppressor molecules in cancer treatment have demonstrated remarkable outcomes and the ability to enhance the advancement of advanced cancers, they may not be appropriate for every patient.[33,34] The therapeutic benefit of the PPI score was further analyzed in two immunotherapy cohorts: the IMvigor 2100 cohort, which involved the intervention of advanced urothelial cancer with the anti-PD-L1 antibody atezolizumab,[35] and the GSE78220 cohort from GEO, which focused on the treatment of metastatic melanoma with the anti-PD-1 antibody pembrolizumab.[36]

To forecast clinical responses to immune checkpoints, the TIDE algorithm[37] and Subclass mapping[38] were employed for the estimation of tumor immune dysfunction and exclusion. Predictions of the response to chemotherapy were also made for every sample using the most extensive pharmacogenomic database accessible to the public (Genomics of Drug Sensitivity in Cancer [GDSC], https//www.cancerrxgene.org/).[39] Table S1 listed a total of 149 medications with the capability to address cancer. The R software's "pRRophetic" package was utilized for making predictions. The package utilized ridge regression to calculate the IC50 values of the samples and evaluated the prediction accuracy through 10-fold cross-validation using the GDSC training set.[40]

3 | RESULTS

3.1 | The genetic variation of PRGs in head and neck cancer is reflected in the landscape

In this study, a total of 33 PRGs were ultimately discovered. Out of the 506 samples, a total of 127 exhibited mutations in m6A regulatory genes, accounting for a prevalence rate of 25.10%. In HNSC samples (Figure 1A), CASP8 displayed the highest mutation frequency, with NIRP3 following closely. Notably, TNF, PJVK, and GSDME, which are involved in prognosis regulation, exhibited no mutations. In the examination of CNV modification occurrence, a dominant CNV modification was observed in 33 regulatory genes, with the majority of genes being linked to copy number amplification. However, cysteinyl aspartate protease (caspase or CASP) family genes like CASP8, CASP4, and CASP1 exhibited a widespread occurrence of CNV deletion (Figure 1B). Figure 1C displays the position of CNV modification of PRGs on chromosomes. Figure 1D clearly showed that HNSC samples were completely differentiated from normal samples based on the expression of the 33 PRGs. An abnormal elevation of most PRGs was observed in tumor samples when compared to normal samples, except for CASP9, ELANE, IL18, and IL6 (Figure 1E). To assess the reciprocal control among the PRGs, a Spearman correlation analysis was conducted (see Figure S1). Other

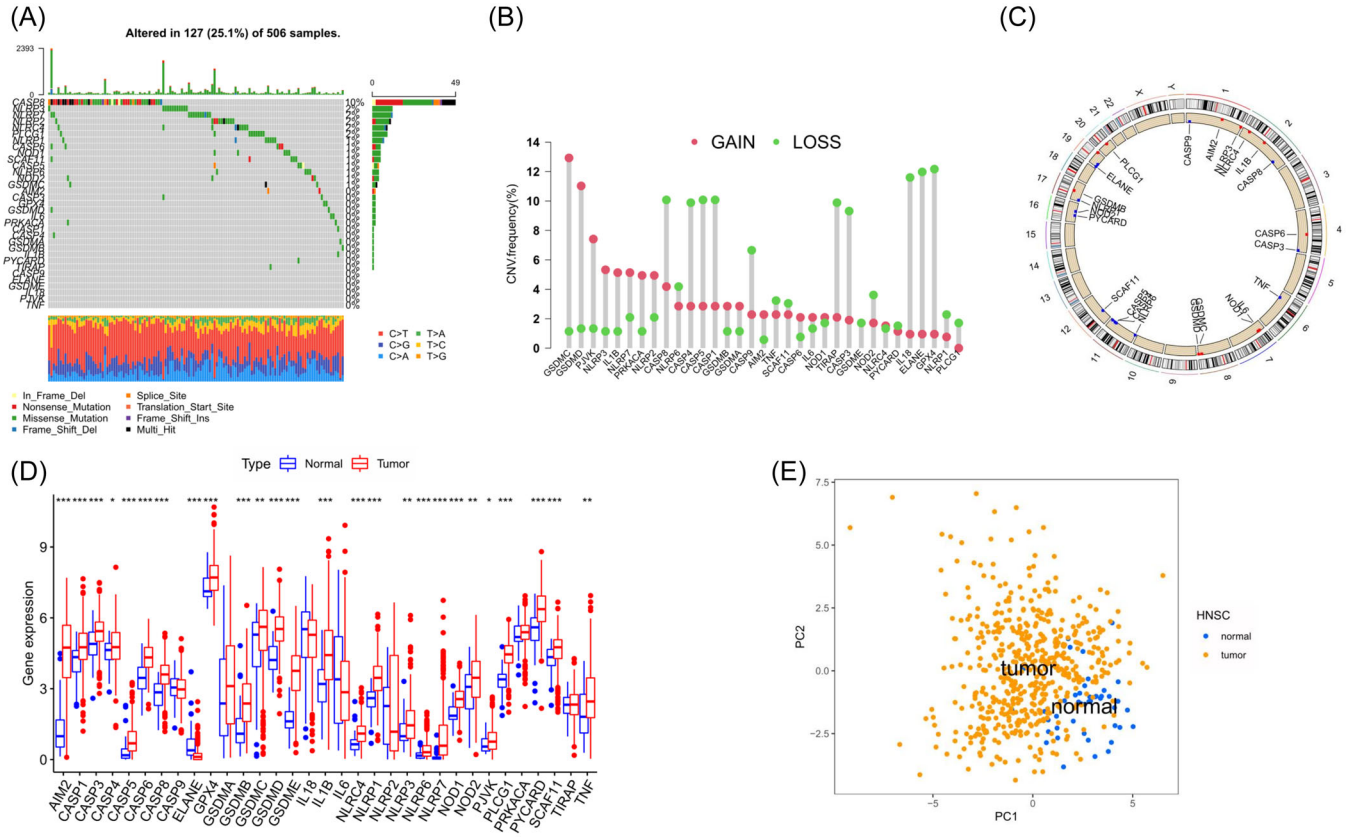

FIGURE 1 Landscape of genetic and expression variation of pyroptosis-related genes (PRGs) in head and neck cancer. (A) The mutation frequency of 33 PRGs in 502 patients with head and neck cancer from the TCGA-HNSC cohort. The number on the right indicated the mutation frequency in each PRG. Each column represented an individual patient. (B) The CNV variation frequency of PRGs in the TCGA-HNSC cohort. The height of the column represented the alteration frequency. The deletion frequency, blue dot; the amplification frequency, red dot. (C) The location of the CNV alteration of PRGs on the chromosomes. (D) Principal component analysis of PRGs to distinguish tumors from normal samples. (E) The difference of messenger RNA expression levels of 33 PRGs between normal and HNSC samples.

PRGs exhibited a notable and positive correlation with CASP5. In general, the findings indicated that there is significant diversity in the genetic and expression patterns of PRGs between normal and HNSC samples, suggesting that the expression of PRGs plays a crucial part in the onset and progression of HNSC.

3.2 | Identification of pyroptosis-related molecular subtypes

In the meta-GEO cohort, we deemed six GEO datasets (LHNG cohort/GSE65858, GSE41613, GSE39366, GSE31056, GSE30784, and GSE27020) as suitable, as they had clinical data available. The prognostic values of the 33 PRGs in patients with HNSC were revealed using a univariate Cox regression model and the Kruskal–Wallis test (Figure S2A,B; Table S2). The PRG network (Figure 2A) demonstrates the synthesis of the connections, interactions, and prognostic importance of the 33 PRGs in HNSC patients. The discovery indicated that the interaction among PRGs might have a significant impact on the development of pyroptosis alteration patterns and the characterization of TME cell infiltration in distinct tumors. Using the aforementioned assumptions, the consensus cluster analysis was employed to categorize samples into distinct groups with varying pyroptosis alterations, depending on the 33 PRGs' expression. Figures 2B and S3A–C revealed the identification of three separate clusters of modification patterns, consisting of 197 patients in Cluster I, 727 samples in Cluster II, and 286 cases in Cluster III. The three clusters were compared using Kaplan–Meier survival analysis, and the log rank test was employed to determine the significant disparity in survival time. The study revealed that individuals belonging to gene cluster III exhibited a more favorable prognosis, whereas those in gene cluster I had an unfavorable prognosis for OS (based on the log rank test, with a significance level of $p < 0.05$; as shown in Figure 2C). In addition, the TCGA-HNSC group was confirmed and yielded comparable outcomes (log rank analysis, $p < 0.05$; Figure 2D). Using PCA, the expression profiles of the 33 PRGs were analyzed to identify three subgroups in the meta-GEO cohort (Figure 2E).

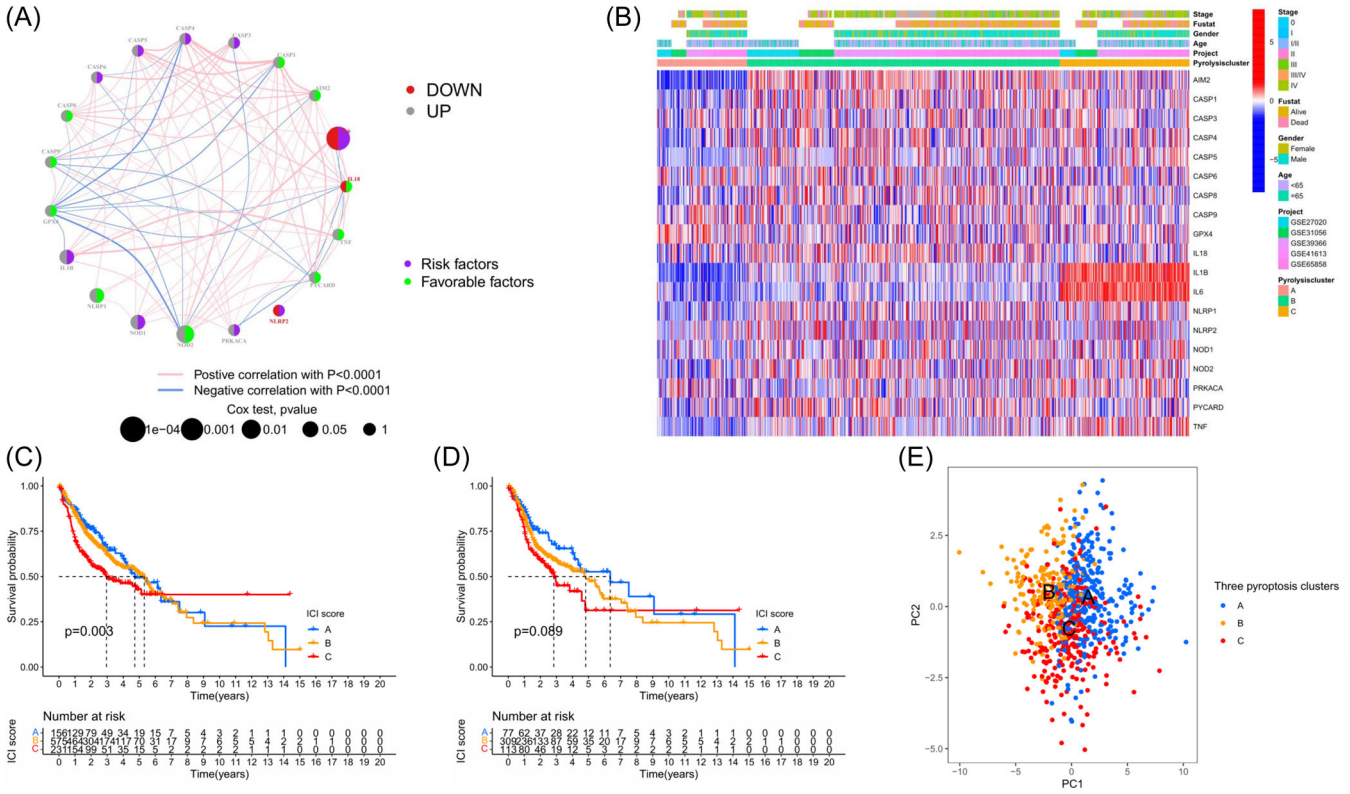

FIGURE 2 Patterns of pyroptosis modification in HNSC. (A) The interaction between 33 PRGs in head and neck cancer. The size of circles represented the effect of each PRG on the prognosis, and the range of values calculated by the lo rank test was $p < 0.001$; $p < 0.01$; $p < 0.05$; $p < 0.1$, respectively. Green dots in the circle, risk factors of prognosis; black dots in the circle, protective factors of prognosis. The lines linking PRGs showed their interactions, and thickness showed the correlation strength between PRGs. A negative correlation was marked with blue and a positive correlation with red. (B) Unsupervised clustering of 33 PRGs in five independent HNSC cohorts. (C) Kaplan–Meier curves of overall survival (OS) for 939 HNSC patients in the meta-GEO cohort with different pyroptosis clusters. (D) Kaplan–Meier curves of OS for 394 HNSC patients in the TCGA HNSC cohort with three pyroptosis clusters. (E) Principal component analysis of three pyroptosis clusters to distinguish tumors from each other.

3.3 | The infiltration properties of immune cells from the TME in the three clusters associated with pyroptosis

To reveal the biological role of the pyroptosis-related clusters, an analysis of GSVA enrichment was performed. According to GSVA, Cluster A showed significant enrichment in pathways associated with energy metabolisms, such as CITRATE_CYCLE_TCA_CYCLE, PEROXISOME, and FATTY_ACID_METABOLISM. On the other hand, Cluster B exhibited significant enrichment pathways linked to cancer activation and stromal pathways, including the NOD_LIKE_RECEPTOR_SIGNALING_PATHWAY, RIG_I_LIKE_RECEPTOR_SIGNALING_PATHWAY, T_CELL_RECEPTOR_SIGNALING_PATHWAY, and NATURAL_KILLER_CELL_MEDIATED_CYTOTOXICITY. Interestingly, Cluster C exhibited a significant enrichment in metabolic regulation and signaling pathways related to the stroma (Figure 3A–C).

Using the ssGSEA algorithm, we systematically assessed the TME cell infiltration models and TME signatures in the three ICI clusters. Figure 3D displayed the heatmap of 28 subpopulations of immune infiltrating cells within pyroptosis-associated clusters. Cluster A exhibited a significant presence of B cells that were extremely inexperienced, CD8 T cells, follicular helper T cells, regulatory T cells (Tregs), activated natural killer (NK) cells, monocytes, M0 macrophages, and resting mast cells among the three subtypes. Group B patients exhibited a notably elevated abundance of T cells CD4 memory resting, M1 and M2 macrophages, dendritic cells resting, stromal score, and immune score. Cluster C subjects exhibited a notable rise in the infiltration of plasma cells. In addition, CIBERSORT, an algorithm that employs support vector regression to assess immune cell subpopulations in the TME, was employed to provide further insights into immune infiltration within the three subpopulations. Figure S4 also showed similar findings. Hence, there is speculation that the activation of stroma in Cluster B hinders the immune cells' ability to suppress tumor growth. The additional examination also verified that stromal stimulation in the Cluster B subtype was greatly intensified, and the mechanisms associated with cell death, the pathway of signaling through toll-like receptors, and the pathway of signaling through T cell receptors were demonstrated, providing further validation of our supposition.

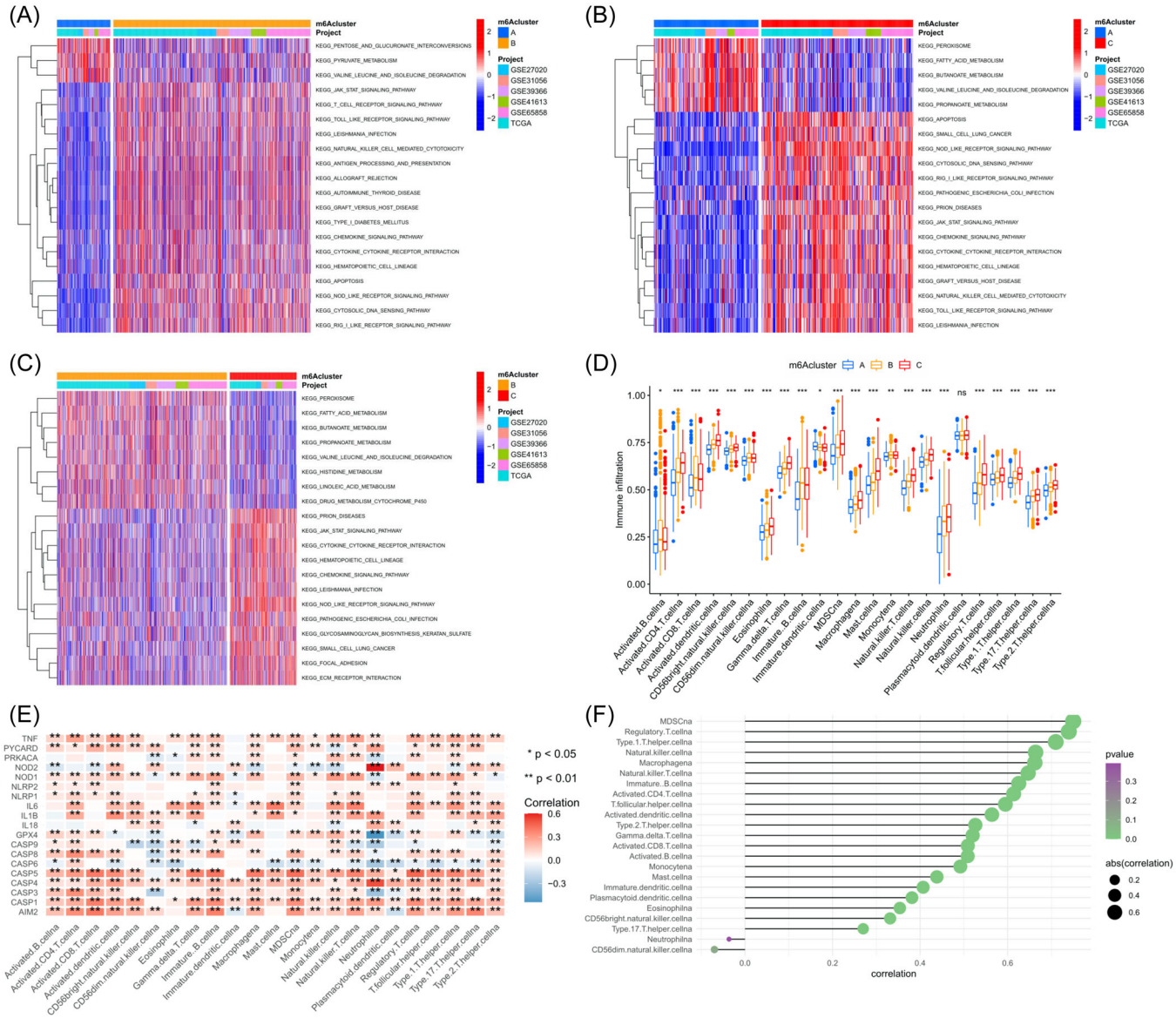

FIGURE 3 Pyroptosis modification and relevant biological pathway. (A–C) GSVA enrichment analysis showing the activation states of biological pathways in three pyroptosis clusters. The heatmap was used to visualize these biological processes; yellow represented activated pathways and blue represented inhibited pathways. HNSC cohorts were used as sample annotations. (A) Pyroptosis cluster A versus pyroptosis cluster B; (B) pyroptosis cluster B versus pyroptosis cluster C; (C) pyroptosis cluster A versus pyroptosis cluster C. (D) Differences in tumor-infiltrating immune cells between the three clusters. (E) Cellular interaction of tumor-infiltrating immune cell types. (F) NLRC4 has a significant positive correlation with prognosis and immune infiltration.

Spearman's correlation analyses (Figure 3E) were conducted to investigate the precise association between every type of TME infiltration cell and each PRG. Enhanced ICI showed a significant correlation with the high expression of several PRGs like CASP family members and NOD2, while neutrophil infiltration levels were negatively correlated with the expression of GPX4, CASP3, and CASP6. NLRC4 caught our interest among these PRGs due to its notable association with prognosis and immune infiltration, as depicted in Figure 3F.

3.4 | DEGs associated with pyroptosis in head and neck cancer

The "limma" package of the R software was used to determine the transcriptomic variation between different pyroptosis phenotypes. The empirical Bayesian approach (Figure 4A) was used to analyze the 1276 DEGs that were common to the three clusters. Figure 4B,C illustrates that DEGs were concentrated in immune-related Gene Ontology categories, such as T cell stimulation,

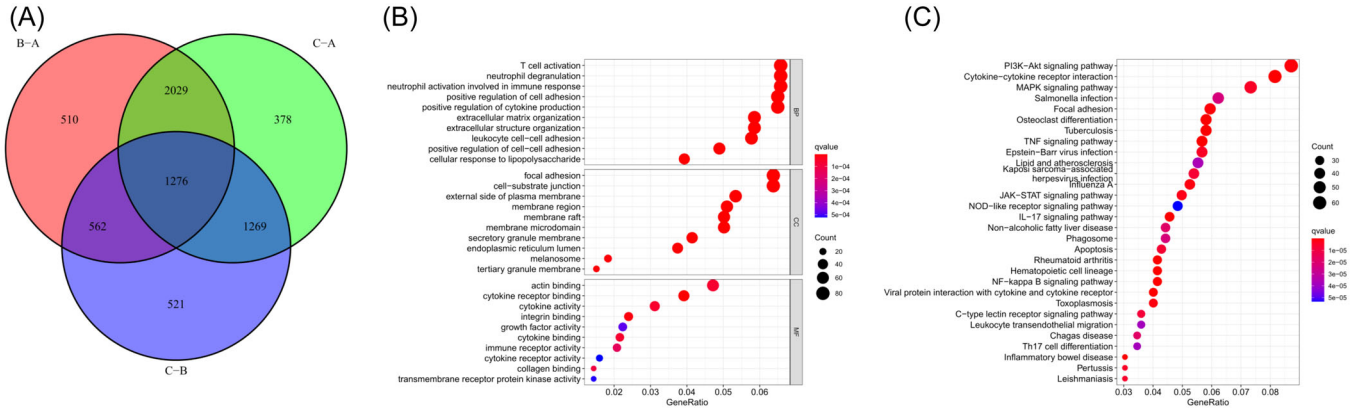

FIGURE 4 Construction of pyroptosis-related differentially expressed gene (DEG) signatures and functional annotation. (A) Venn diagram of 1276 pyroptosis-related DEGs between three pyroptosis clusters. (B) Functional annotation for PRGs using Gene Ontology GO enrichment analysis. (C) Functional annotation for PRGs using the Kyoto encyclopedia of genes and genomes (KEGG) enrichment analysis.

release of neutrophil contents, immune receptor function, and neutrophil activation in immune response. In addition, they were also found in pathways associated with immune/cancer interactions, including the TNF signaling pathway, the IL-17 signaling pathway, the NF-kappa B signaling pathway, the PI3K-Akt signaling pathway, and the differentiation of Type 17 T helper cells (Th17).

Out of these DEGs, a total of 545 DEGs were recognized as prognostic genes according to Table 1. The prognostic DEGs were then analyzed by the unsupervised clustering method. In the meta-GEO cohort, three genomic clusters, specifically gene Clusters A, B, and C, were discovered. Figure 5A displayed the transcriptome profiles of the DEGs within the three genomic clusters, as depicted by the heat map. In gene cluster C, among the 33 PRGs, AIM2, CASP1, CASP4, CASP8, GSDMD, GSDME, IL1B, IL6, NLRP1, NOD1, PLCG1, and TNF showed significant upregulation. On the other hand, gene cluster A exhibited upregulation of CASP3, CASP6, CASP9, GPX4, GSDMB, and PRKACA. Aberrant expression of GSDMA, GSDMC, IL18, NOD2, PYCARD, and SCAF11 was observed in gene Cluster B (Figure 5B). Next, the examination focused on the particular association between every type of TME infiltration cell and each PRG. Gene Cluster A exhibited elevated levels of stimulated B cell, eosinophil, stimulated CD8 T cell, and regulatory T cell. Figure 5C showed that Gene cluster C exhibited enrichment of activated CD4 T cell, activated dendritic cell, CD56 bright NK cell, CD56 dim NK cell, gamma delta T cell, immature B cell, MDSC, macrophage, mast cell, monocyte, NK T cell, NK cell, regulatory T cell, Th1 cell, Th17 cell, and Th2.

According to survival analysis, patients with gene cluster C exhibited a more favorable prognosis, whereas those with gene cluster A showed an unfavorable prognosis for OS (log rank test, $p < 0.001$; Figure 5D). Furthermore, it was noted that individuals with a progressed clinical phase were characterized by the gene Cluster B subgroup, while those exhibiting decreased PD-L1 expression were predominantly found in gene Cluster B and C subgroups (Figure 5E). The results also indicated that stratifications exhibited distinct clinicopathologic characteristics and were identified as gene Clusters A, B, and C (Figure 5F,G,I). The regulatory genes showed notable variations among the three subgroups of PRGs signature, aligning with the anticipated outcomes of the pyroptosis modification pattern.

3.5 | Establishment of the PPI index and exploration of its clinical relevance

While our results validate the involvement of pyroptosis in prognosis and regulation of immune invasion, it is important to note that these analyses were solely conducted on patient populations and did not provide an accurate prediction of the alteration of pyroptosis in an individual tumor. Hence, an indicator of future outcomes score was formulated and designated as the PPI index relying on the PCA algorithm. The meta-GEO cohort patients were divided into two categories based on their PPI scores, using the most accurate threshold values. Figure 6A illustrates the allocation of patients among the three gene clusters. Figure 6B also assessed the correlation between established immune signatures and the PPI score to provide a clearer depiction of the PRG signature's characteristics. In Figure 6C, pyroptosis Cluster A exhibited a greater PPI compared to Cluster C and Cluster B, while in Figure 6D, gene Cluster A displayed a higher PPI than Cluster C and Cluster B. Spearman's correlation analysis was utilized to investigate the association between identified biological traits and PPI scores. The scatter diagram indicated a significant positive correlation between PPI scores and cell cycle regulators (Figure 6E) as well as the WNT pathway (Figure 6F) while displaying a negative correlation with mismatch repair (Figure 6G) and angiogenesis (Figure 6H).

TABLE 1 Prognostic genes of pyroptosis-related DEGs in the meta cohort.

ID	HR	HR.95L	HR.95H	*p* Value
XYLT2	1.29691	1.076004	1.56317	0.006355
LARP6	1.266636	1.125973	1.424873	8.31E−05
NOX4	1.139376	1.026343	1.264857	0.014376
COL10A1	1.062942	1.008538	1.120282	0.02278
SULF1	1.077868	1.010165	1.150109	0.02348
ACVR1	1.159116	1.002066	1.34078	0.046839
FOXF2	1.14116	1.023744	1.272041	0.017146
EGLN3	1.086472	1.002792	1.177135	0.042544
P4HA1	1.476689	1.304708	1.67134	6.83E−10
STC2	1.271687	1.160355	1.3937	2.72E−07
HOXC6	1.113041	1.001791	1.236646	0.046232
GLG1	1.256676	1.03427	1.526907	0.021503
CDH11	1.098933	1.018988	1.185149	0.014362
TGM1	0.941318	0.895893	0.989046	0.016556
LAMB3	1.125807	1.030175	1.230318	0.008888
APP	1.25389	1.096859	1.433403	0.000919
ARL4C	1.146228	1.018068	1.29052	0.024072
NID1	1.164153	1.061618	1.276592	0.001233
SERPINE2	1.127064	1.044853	1.215743	0.001966
DKK3	1.181	1.068068	1.305873	0.001178
MAGEH1	1.139605	1.004257	1.293195	0.042784
MMP13	1.051916	1.012552	1.09281	0.009295
LHFPL2	1.166791	1.011219	1.346297	0.03462
GNA12	1.428293	1.209139	1.687169	2.73E−05
PTK7	1.193968	1.039851	1.370925	0.011932
KLK12	0.931325	0.888362	0.976367	0.003152
FARP1	1.14206	1.002505	1.301041	0.045761
LRP12	1.226166	1.089555	1.379907	0.000717
TMEM184B	1.330451	1.11395	1.58903	0.001628
TPST1	1.205569	1.078002	1.348231	0.001052
CSTB	0.861523	0.785539	0.944856	0.001556
TRAM2	1.161685	1.011715	1.333886	0.033577
MAP1B	1.130082	1.027339	1.2431	0.011918
CRNN	0.965201	0.934299	0.997124	0.032891
NEDD9	1.212145	1.081247	1.35889	0.000968
DSG2	1.113117	1.024583	1.209302	0.011268
HSP90B1	1.360787	1.118377	1.65574	0.002086
ETS1	1.147718	1.01515	1.297599	0.027802
TGM3	0.947095	0.914268	0.981102	0.002528
DPY19L1	1.180051	1.021605	1.363073	0.024416
INHBB	1.18258	1.087874	1.285531	8.23E−05
NFE2L1	1.241567	1.049791	1.468376	0.011485
PPL	0.881535	0.819119	0.948707	0.000765
INHBA	1.184569	1.102599	1.272634	3.67E−06
MMP2	1.111267	1.015929	1.215552	0.021151
RAB25	0.868311	0.806203	0.935204	0.000192
PLAUR	1.228336	1.099381	1.372416	0.000279
LITAF	1.186823	1.00714	1.398562	0.040864
MSC	1.200947	1.094987	1.31716	0.000102
SOAT1	1.276423	1.096193	1.486287	0.001675
ATP2B4	0.832925	0.706825	0.981523	0.029063
CHPF	1.269965	1.110793	1.451945	0.000469
PTPRR	1.253903	1.026589	1.531549	0.026616
CSTA	0.853663	0.797013	0.91434	6.30E−06
PITX1	0.802528	0.73286	0.878818	2.05E−06
SLC16A6	0.870687	0.76798	0.98713	0.030601
ALS2CL	0.860694	0.756226	0.979593	0.02307
MICAL2	1.219536	1.080396	1.376596	0.001323
MSN	1.173952	1.018028	1.353757	0.027405
BCAT1	1.121793	1.030633	1.221017	0.007867
EVPL	0.85879	0.786391	0.937854	0.000704
GLTP	0.819513	0.741	0.906345	0.000107
TGFBI	1.120726	1.045805	1.201016	0.001244
ANXA5	1.535987	1.298945	1.816288	5.21E−07
FUT6	0.843177	0.767389	0.92645	0.000386
DENND2D	0.726704	0.626423	0.843038	2.51E−05
AXL	1.203911	1.078942	1.343355	0.000904
ZNF639	1.259112	1.06078	1.494527	0.008422
CYB5R3	1.260687	1.017797	1.561539	0.033878
PDIA6	1.221262	1.03442	1.441853	0.018304
CNIH3	1.209005	1.019001	1.434439	0.029575
APLP2	1.266795	1.075523	1.492083	0.004629
MAL	0.960304	0.923745	0.99831	0.040817
CALML5	0.877656	0.840766	0.916165	2.58E−09
SCEL	0.926024	0.876468	0.978382	0.006166
GABARAPL1	1.193956	1.0504	1.35713	0.006682
NRSN2	1.23226	1.062689	1.42889	0.005694

TABLE 1 (Continued)

ID	HR	HR.95L	HR.95H	*p* Value
DDOST	1.349804	1.071605	1.700226	0.010858
SPINK5	0.887729	0.845668	0.931881	1.52E−06
PTDSS1	1.277505	1.080392	1.51058	0.004179
NDRG1	1.11878	1.012763	1.235895	0.027131
TM7SF2	0.888298	0.813305	0.970206	0.008486
FUT3	0.882012	0.81581	0.953587	0.001612
CTSZ	1.141007	1.011762	1.286763	0.031508
TWSG1	1.204773	1.040692	1.394723	0.012634
TPM1	1.181625	1.076333	1.297218	0.000457
CLSTN2	1.127845	1.008545	1.261257	0.034934
SNX10	1.16279	1.043032	1.296298	0.006534
ERF	1.227076	1.02442	1.469822	0.026288
OLR1	1.186432	1.098566	1.281325	1.33E−05
ZNF281	1.407943	1.20498	1.645093	1.65E−05
TOR1A	1.654326	1.301684	2.102503	3.86E−05
RASAL1	0.866299	0.762803	0.983837	0.027037
SCG5	1.232138	1.148495	1.321872	5.88E−09
ARPC1B	1.163229	1.001602	1.350937	0.047598
TMED2	1.410183	1.151511	1.726962	0.000886
CYP2C18	0.875504	0.819944	0.934829	7.05E−05
EFEMP1	1.10013	1.001424	1.208565	0.046632
LY6G6C	0.927623	0.874811	0.983623	0.012002
STX2	1.35379	1.137977	1.610531	0.000629
LASP1	1.376742	1.118076	1.695251	0.002603
NMU	0.901952	0.844897	0.96286	0.001967
HOPX	0.873536	0.808728	0.943537	0.000587
ST3GAL2	1.22066	1.010487	1.474548	0.038624
JAM3	1.145645	1.005789	1.304948	0.040672
MT1F	1.298073	1.159978	1.452607	5.47E−06
PRKAB2	1.175324	1.011677	1.365442	0.03471
TNFRSF12A	1.240456	1.128225	1.363851	8.45E−06
SCG2	1.195768	1.110423	1.287672	2.22E−06
ALDH1B1	1.244187	1.108113	1.39697	0.000218
ALOX12	0.926048	0.863976	0.992579	0.029978
FAM135A	0.812141	0.706951	0.932984	0.003281
SIRT7	0.786733	0.630071	0.982347	0.034246
TREM1	1.151536	1.063599	1.246743	0.000499
NCF2	1.177597	1.051464	1.318861	0.004682
NLRX1	0.813027	0.700135	0.944122	0.006651
TTC9	0.841095	0.761679	0.928792	0.000627

TABLE 1 (Continued)

ID	HR	HR.95L	HR.95H	*p* Value
THBS1	1.31116	1.213337	1.41687	7.49E−12
SPRR3	0.932931	0.902859	0.964004	3.28E−05
RAPGEFL1	0.855302	0.786697	0.929891	0.000248
ATP6V1C1	1.442359	1.176376	1.768483	0.000429
ABLIM1	0.787821	0.701411	0.884876	5.74E−05
MPP1	1.226327	1.068634	1.407291	0.00367
KLF10	1.213793	1.060158	1.389691	0.005016
PIK3IP1	0.85421	0.747616	0.976001	0.020495
ALDH18A1	1.222674	1.021979	1.462781	0.027977
LLGL2	0.745525	0.639405	0.869256	0.000178
SLC39A8	1.136591	1.002131	1.289093	0.04625
KLK10	0.944836	0.893685	0.998913	0.04569
SLC25A10	0.745121	0.631843	0.878707	0.000471
CD63	1.514009	1.260224	1.8189	9.39E−06
TIAM1	0.787827	0.687622	0.902635	0.000591
NDFIP1	1.517489	1.195944	1.925486	0.000597
PSCA	0.924598	0.867642	0.985293	0.015662
KLK11	0.92953	0.879525	0.982379	0.009595
BSPRY	0.838713	0.771977	0.911218	3.21E−05
TINAGL1	1.21401	1.101211	1.338363	9.71E−05
GFPT2	1.178785	1.075027	1.292557	0.000467
PANX1	1.146005	1.00944	1.301045	0.035283
SFXN3	1.351727	1.147802	1.591883	0.000304
LYPD3	0.861532	0.804805	0.922257	1.80E−05
ERBB3	0.768161	0.670993	0.879399	0.000132
KBTBD2	1.283048	1.050985	1.566352	0.014346
LGALS1	1.23354	1.120066	1.35851	2.02E−05
ZNF750	0.87818	0.821586	0.938672	0.000132
FHL2	1.275099	1.130784	1.437832	7.32E−05
DBI	0.76199	0.645226	0.899884	0.00136
OVOL1	0.893804	0.812772	0.982914	0.020592
HSPA4L	0.859612	0.776346	0.951809	0.003613
EPHX2	0.858396	0.776478	0.948956	0.002847
MGAT1	1.371482	1.110695	1.6935	0.003329
DBNDD1	0.882103	0.78301	0.993737	0.039084
SCNN1A	0.87176	0.813248	0.934481	0.000108
ITGA3	1.1501	1.041548	1.269966	0.005697
CYP2C9	0.799505	0.669947	0.954118	0.013114
NUDCD3	1.413573	1.092916	1.828308	0.008368

(Continues)

TABLE 1 (Continued)

ID	HR	HR.95L	HR.95H	*p* Value
GDPD5	1.218913	1.033698	1.437314	0.018568
CTSB	1.174501	1.026233	1.344191	0.019489
SH2B3	1.149417	1.006717	1.312344	0.039499
TSPO	0.705501	0.578377	0.860565	0.000579
CES3	0.825806	0.694592	0.981808	0.030165
SIL1	1.535338	1.250923	1.884419	4.10E−05
FNDC3A	1.242389	1.048914	1.471552	0.011975
HDAC9	1.413298	1.174284	1.700961	0.000253
GIPC1	0.785315	0.635383	0.970626	0.025366
CANX	1.348199	1.103924	1.646527	0.003396
GLS	1.209414	1.047557	1.396278	0.009493
HOXA1	1.330354	1.161726	1.523459	3.66E−05
RGS19	1.27153	1.053432	1.534783	0.012344
SAMD4A	1.278198	1.141071	1.431805	2.24E−05
DUOX1	0.881145	0.801205	0.969061	0.009117
PRSS12	0.807898	0.738412	0.883923	3.34E−06
ARHGEF7	1.290341	1.010404	1.647836	0.04106
KTN1	1.286827	1.095467	1.511616	0.002141
ENSA	0.733579	0.579666	0.928359	0.009918
NTAN1	1.278397	1.011764	1.615297	0.039594
NTRK2	0.930127	0.874504	0.989289	0.021321
EPN3	0.838107	0.742247	0.946347	0.004375
LCN2	0.931653	0.887539	0.97796	0.00423
MAPK13	0.864323	0.77396	0.965237	0.009655
CRYM	0.888664	0.800426	0.986629	0.02695
PSD3	0.876018	0.779679	0.984261	0.025957
ULBP1	1.188275	1.045271	1.350843	0.008371
ICAM1	1.101498	1.003607	1.208937	0.041772
NRIP1	1.137867	1.014004	1.27686	0.028058
CAMK2N1	1.329294	1.214886	1.454477	5.68E−10
MRAS	1.154194	1.022469	1.30289	0.020377
POMT2	1.356344	1.08254	1.699399	0.008065
SLC25A32	1.344068	1.118813	1.614675	0.00158
CEACAM1	0.90788	0.839326	0.982034	0.015842
PLCD1	0.789141	0.684276	0.910077	0.001133
FSTL3	1.21902	1.119181	1.327765	5.56E−06
ADA	1.451826	1.277885	1.649443	1.03E−08
RNF14	1.394559	1.092437	1.780236	0.007593
BCAR3	1.29701	1.167982	1.44029	1.15E−06

TABLE 1 (Continued)

ID	HR	HR.95L	HR.95H	*p* Value
RABGGTB	1.259644	1.013218	1.566003	0.037692
EMP3	1.14563	1.020103	1.286602	0.021669
SASH1	0.87454	0.786825	0.972034	0.01292
SPRR1A	0.929043	0.891527	0.968138	0.000466
TRIM32	1.516757	1.292418	1.780037	3.38E−07
CEBPB	1.275988	1.095249	1.486553	0.001763
RAB31	1.162093	1.027721	1.314034	0.01657
PAX9	0.883506	0.81241	0.960825	0.003808
CYP2C19	0.374608	0.157314	0.892044	0.026553
ATG12	1.377945	1.076558	1.763707	0.010905
IVL	0.929627	0.881849	0.979994	0.006715
TNPO1	1.297919	1.060612	1.588324	0.011368
WNT4	0.876398	0.79441	0.966848	0.00847
ILK	1.273212	1.069984	1.515041	0.006482
IL21R	0.808876	0.703571	0.929941	0.002876
SLC20A1	1.30057	1.126854	1.501066	0.000327
CD300C	1.213318	1.035551	1.421601	0.01675
B4GALT3	1.729395	1.369255	2.18426	4.27E−06
SPRR1B	0.946396	0.904443	0.990295	0.017241
CAV1	1.11067	1.024164	1.204484	0.011178
CHST11	1.193421	1.064028	1.338549	0.002529
IL2RB	0.884235	0.808694	0.966833	0.006929
PTPRE	1.221373	1.040914	1.433116	0.014224
DYSF	1.170588	1.046729	1.309103	0.005774
DLX5	0.889593	0.811969	0.974637	0.012023
STAP2	0.745028	0.649938	0.85403	2.39E−05
PTPN13	0.793361	0.716558	0.878396	8.36E−06
FUT2	0.786835	0.709738	0.872307	5.20E−06
PXN	1.392276	1.20364	1.610476	8.38E−06
CDS1	0.857526	0.756304	0.972296	0.016469
MTMR6	1.301271	1.059251	1.598588	0.012134
PEA15	1.351756	1.08901	1.677895	0.006272
CFL1	1.25947	1.025175	1.547312	0.028041
PGAP1	0.798501	0.688303	0.926342	0.00298
ACP2	1.220475	1.013312	1.469989	0.03579
HTR7	1.147172	1.031092	1.27632	0.011653
IGFBP2	0.923603	0.869325	0.98127	0.010116
DSE	1.220392	1.073382	1.387536	0.002356
SPCS3	1.419239	1.172052	1.718559	0.000336

TABLE 1 (Continued)

ID	HR	HR.95L	HR.95H	*p* Value
LAD1	0.886266	0.788615	0.99601	0.042654
NOD1	1.35881	1.07148	1.723191	0.011421
APOE	1.085117	1.008283	1.167807	0.02925
TGM5	0.889898	0.81118	0.976254	0.013567
FLII	1.295056	1.044068	1.606381	0.018657
TACSTD2	0.82502	0.729514	0.93303	0.002182
SERPINA1	1.108649	1.017782	1.207629	0.018082
SLC9A3R1	0.829647	0.741314	0.928507	0.001148
CEACAM5	0.916182	0.87293	0.961577	0.000388
SPTBN2	0.835372	0.738075	0.945495	0.004413
BMP7	0.92411	0.856026	0.99761	0.043254
GNRHR	0.715716	0.547437	0.935722	0.014454
VASP	1.240091	1.014248	1.516224	0.035915
FGFR2	0.822351	0.732041	0.923801	0.000983
APPL2	0.805459	0.6805	0.953363	0.011896
PVR	1.495225	1.242913	1.798756	1.99E−05
POPDC3	1.134423	1.064587	1.20884	1.00E−04
PRUNE2	1.127257	1.03603	1.226518	0.005402
DUOX2	0.887911	0.822443	0.95859	0.002349
ACO1	1.241225	1.042726	1.47751	0.015076
RNF121	1.299652	1.096719	1.540135	0.00248
TRIM29	0.819545	0.74933	0.89634	1.33E−05
NTF3	0.774544	0.654953	0.915971	0.002829
DSG1	0.946231	0.909674	0.984258	0.005973
VEGFC	1.184812	1.104304	1.27119	2.32E−06
ARHGAP29	1.309174	1.138061	1.506014	0.000164
PLXNA2	0.808917	0.698084	0.937347	0.004794
FADS3	1.316445	1.181131	1.467262	6.76E−07
ECHDC2	0.793552	0.707792	0.889704	7.41E−05
STK10	1.214303	1.011303	1.458053	0.03749
ERBB2	0.730551	0.618231	0.863277	0.000228
SMAD6	0.786044	0.633583	0.975192	0.028647
SNAP23	1.283683	1.038469	1.586799	0.020945
MPZL2	0.862386	0.775985	0.958407	0.005983
SACS	1.238147	1.066606	1.437277	0.004994
HMGN3	0.806495	0.685501	0.948845	0.009511
FPR1	1.115472	1.017943	1.222346	0.019236
GNPDA1	1.448034	1.152205	1.819817	0.001498
ACTN1	1.34765	1.203247	1.509383	2.47E−07
SGPP1	1.206766	1.052015	1.384281	0.007271

TABLE 1 (Continued)

ID	HR	HR.95L	HR.95H	*p* Value
FLG	0.931548	0.873764	0.993153	0.029988
APOC1	1.071971	1.005067	1.143327	0.034542
TWISTNB	1.286094	1.048884	1.576951	0.015573
LTBP4	0.869115	0.762762	0.990296	0.035171
MRPL15	1.287125	1.073292	1.543561	0.006469
CYP4F12	0.791949	0.718075	0.873424	3.03E−06
MSMB	0.93112	0.883321	0.981506	0.007949
ALOX12B	0.912794	0.863835	0.964529	0.001179
NT5E	1.14313	1.058409	1.234632	0.000662
DLG3	0.799638	0.679232	0.941389	0.007246
DOCK2	0.880404	0.785188	0.987166	0.029172
CBR3	0.858993	0.777351	0.94921	0.002855
ZMAT5	0.789994	0.64945	0.960951	0.01835
ACTB	1.378478	1.112325	1.708315	0.003362
LRRC8D	0.860994	0.745888	0.993864	0.040951
CXADR	0.874655	0.792088	0.965828	0.008115
PLEKHH3	0.695225	0.55854	0.86536	0.001135
SERPINI2	0.652481	0.44222	0.962715	0.031443
VSIG4	1.134556	1.045978	1.230636	0.002336
PNMA1	1.362288	1.171819	1.583716	5.74E−05
ATP10B	0.814037	0.735359	0.901133	7.27E−05
PSEN2	1.411232	1.180407	1.687193	0.000157
DSP	0.874386	0.80356	0.951456	0.001842
TAF7	1.242086	1.011634	1.525036	0.038412
GCHFR	0.844993	0.758276	0.941628	0.002299
MRPL22	1.330421	1.050505	1.684923	0.017848
PELI1	0.848755	0.743583	0.968803	0.015119
BTG3	0.75541	0.649228	0.878957	0.000284
CALML3	0.866027	0.807416	0.928892	5.75E−05
GRB7	0.838471	0.740252	0.949722	0.00558
UFM1	1.568464	1.268364	1.939569	3.27E−05
YKT6	1.326238	1.11229	1.581337	0.001657
MS4A4A	1.104977	1.00836	1.210852	0.032493
FCF1	1.394169	1.144442	1.698388	0.000968
CYP3A5	0.903708	0.825195	0.989692	0.029006
POF1B	0.871354	0.815019	0.931582	5.39E−05
MAP4K4	1.357555	1.137793	1.619764	0.000692
DCUN1D4	1.381508	1.122628	1.700086	0.002269
HOOK1	0.800381	0.717044	0.893403	7.21E−05

(Continues)

TABLE 1 (Continued)

ID	HR	HR.95L	HR.95H	*p* Value
INPP4B	1.264711	1.124329	1.42262	9.15E−05
ITGB3	1.342908	1.110412	1.624085	0.002368
TOR1AIP2	1.46059	1.119275	1.905985	0.005275
ELK3	1.243723	1.060664	1.458377	0.007253
JMJD6	1.839798	1.385036	2.443876	2.57E−05
ANGEL1	1.462939	1.179326	1.814758	0.00054
POLR1E	1.2169	1.011817	1.46355	0.037095
CD177	0.905363	0.844974	0.970068	0.004761
ADAMTS6	1.280755	1.054227	1.55596	0.012713
PLA2G3	0.876249	0.811239	0.946468	0.000783
KRT24	0.925329	0.883956	0.968638	0.000883
TGFBR3	0.869409	0.792133	0.954223	0.003213
PTPRC	0.905981	0.82642	0.993201	0.035253
ZNF787	1.259758	1.001004	1.5854	0.049009
TFPI2	1.13683	1.07384	1.203514	1.04E−05
FHOD1	1.318062	1.117717	1.554317	0.001027
HIBCH	0.791832	0.668322	0.938169	0.006983
RIPK2	1.30418	1.095725	1.552294	0.002801
CD28	0.793107	0.670969	0.937478	0.006595
IL10RA	0.895269	0.809	0.990737	0.032356
PRPSAP1	0.7911	0.658708	0.950102	0.012151
HK3	1.148428	1.029546	1.281036	0.013056
TGFBR2	1.157698	1.023999	1.308853	0.01935
ARMC1	1.265347	1.038826	1.541263	0.019364
EYA2	0.93329	0.874759	0.995737	0.036686
DSC2	0.895156	0.830036	0.965384	0.004051
TMOD1	1.0859	1.008653	1.169063	0.028612
CEACAM6	0.925723	0.881357	0.972323	0.002069
SCNN1B	0.848823	0.785319	0.917463	3.61E−05

Following the assessment of the predictive significance of PPI scores, the meta-GEO cohort was examined to analyze immune activity and tolerance conditions. In Figure 6I, the Wilcoxon test indicated that the high PPI group exhibited significant overexpression of the majority of genes related to immune checkpoints and immune activity. Gene set enrichment analysis (GSEA) revealed that GLYCEROPHOSPHOLIPID_METABOLISM, FATTY_ACID_METABOLISM, and the ERBB_SIGNALING_PATHWAY were significantly enriched in the higher PPI score group, whereas ECM_RECEPTOR_INTERACTION, the JAK_STAT_SIGNALING_PATHWAY, TOLL_LIKE_RECEPTOR_SIGNALING_PATHWAY, NATURAL_KILLER_CELL_MEDIATED_CYTOTOXICITY, and the B_CELL_RECEPTOR_SIGNALING_PATHWAY were enriched in the lower PPI group (Figure 6J).

According to the Kaplan–Meier plotter, patients in the lower PPI score group exhibited significantly reduced OS rates compared to those in the higher PPI score group in the meta-GEO cohort (log rank test, $p < 0.05$; Figure 7A), as well as in GSE31056 (log rank test, $p < 0.05$; Figure 7B), GSE41613 (log rank test, $p < 0.05$; Figure 7C), GSE65858 (log rank test, $p < 0.05$; Figure 7D), and TCGA HNSC (log rank test, $p < 0.05$; Figure 7E) cohorts.

3.6 | Relationship between PPI scores and somatic mutations

Increasing evidence suggests a link between genetic mutations in the tumor genome and the response to immunotherapy. Apart from the expression of PD-L1, TMB serves as a separate biomarker for the response to ICI.[41,42] The presence of genetic mutations in tumors is linked to the effectiveness of immunotherapy in various types of tumors and treatment methods, such as CPIs and cellular-based therapy.[42,43] This is a metric for genetic changes in a tumor and is a significant genomic indicator that is strongly linked to immunotherapy and predicting survival.[44,45] To understand the genetic impact of each PPI subgroup, the relationship between TMB and PPI scores was investigated, given the significant clinical significance of TMB. According to Figure 8A, individuals belonging to the high PPI score subgroup exhibited a notably greater TMB compared to those in the low PPI score subgroup (Wilcoxon test $p < 0.05$). Furthermore, the correlation analysis revealed a significant and positive correlation between PPI scores and TMB (Spearman coefficient $R = 0.35$, $p < 0.05$; Figure 8B). According to the findings in Figure 8C, patients with a low TMB exhibited a superior PPI compared to individuals with a high TMB (log rank test, $p < 0.05$). The analysis of survival, stratified by TMB status, revealed an association between predictions made using PPI scores. Both the high and low TMB subgroups showed significant differences in survival (log rank test, $p < 0.05$ for high TMB and high PPI scores (HH) compared to high TMB and low PPI scores (HL), and low TMB and high PPI scores (LH) compared to low TMB and low PPI scores (LL); Figure 8D). In general, these discoveries indicate that the PPI score could be unrelated to TMB and a reliable gauge of possible factors that can determine the reaction to immunotherapy.

Moreover, maftools[32] were utilized to analyze significantly mutated genes in HNSC samples, comparing the low and high PPI score subgroups. Using a chi-square test, Figure 8E and Table 2 helped identify the 25 driver genes that had the most frequent alterations. Significant differences were observed between the low and high PPI score subgroups for NSD1, PTPRZ1, GRM1, ELMO1, FLNA, VPS13C, CUX2, and PKD1L1 among these genes. The discovery of these findings could

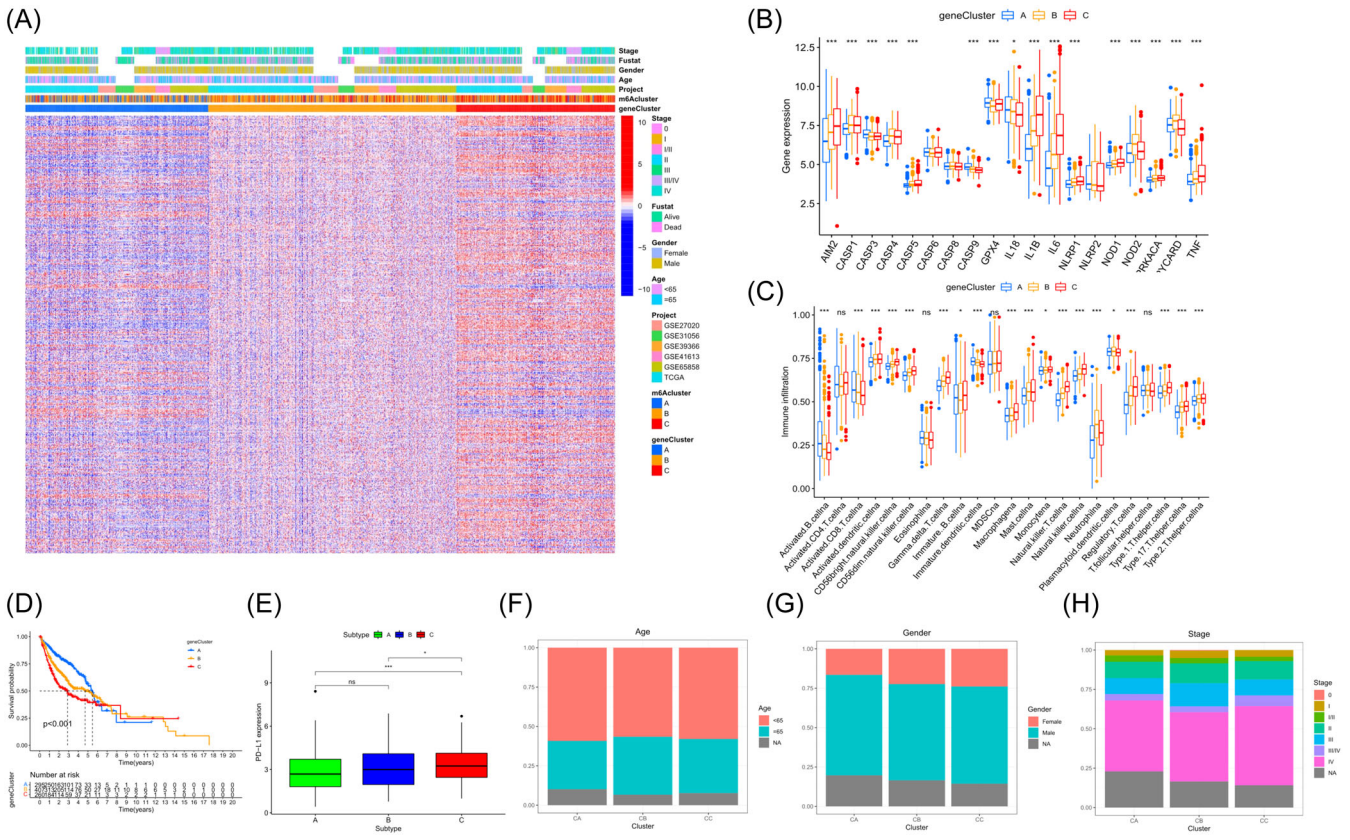

FIGURE 5 Hierarchical clustering of HNSC yields three gene clusters in the meta-GEO cohort. (A) Unsupervised clustering of common DEGs between the three pyroptosis clusters was performed to classify patients into three groups: gene Clusters A, B, and C. (B) Immune-checkpoint-relevant genes (IDO1, CD274, HAVCR2, PDCD1, CTLA4, and LAG3) and immune-activation-relevant genes (CD8A, CXCL10, CXCL9, GZM A, GZMB, PRF1, IFNG, TBX2, and TNF) were expressed in the three gene clusters. (C) Differences in tumor-infiltrating immune cells between the three gene clusters. (D) Kaplan–Meier curves of OS for 939 HNSC patients in the meta-GEO cohort with different gene clusters. (E) Relative distribution of PD-L1 expression in the three gene clusters. (F–H) The distribution of clinical features in the three gene clusters. F, Age; G, Gender; H, Pathological stage.

offer fresh perspectives on the processes of tumor PPI composition and gene mutation in immune checkpoint blockade treatment.

3.7 | PPI score for response to immunotherapy

We assessed the correlation between clinical characteristics and established PPI scores. The advanced TNM stage (Figure 9A,B) was correlated with high PPI scores. The analysis of survival, stratified by PPI scores, indicated a correlation with survival outcomes (Figure 9C,D). Furthermore, there was a positive correlation between higher PPI scores and objective response to therapy in the meta-GEO cohort, as depicted in Figure 9E,F. In the meantime, stratified survival analysis indicated a correlation between the PPI and the outcome success of the primary therapy. Among patients with partial/complete response, high PPI scores were related to worse survival, similar results were obtained among patients with stable/progressive disease (Figure 9G,H).

Despite not being approved as a conventional treatment for HNSC, immunological checkpoint medications were assessed using the submap algorithm to estimate the probability of immunotherapy response in the meta-GEO cohort. The findings revealed that individuals with high PPI scores were more likely to exhibit a favorable response to immunotherapy compared to those with low PPI scores ($p < 2.2e{-}16$). Furthermore, immunotherapy yielded more favorable outcomes in individuals with high PPI scores as per the TIDE algorithm ($p < 0.05$). The findings indicated that individuals with elevated PPI scores exhibited strong responsiveness to programmed cell death 1 (PD1) immunotherapy ($p < 0.05$ after Bonferroni correction) (Figure 10A). Treating patients with HNSC often involves the use of anticancer medication as a fundamental therapeutic approach. The purpose of the PPI model was to evaluate the reaction to antitumor medications in two molecular subcategories using the GDSC cell line dataset. The accuracy of the method's prediction was validated using 10-fold cross-validation, while the IC50 was utilized to estimate the sensitivity of the response. Out of the 130 categories of anticancer medication reactions, 74 drugs exhibited variances among the two PPI clusters as indicated in Table 3. The findings indicated that elevated PPI scores exhibited greater responsiveness to 68 different types of medications in comparison to lower PPI

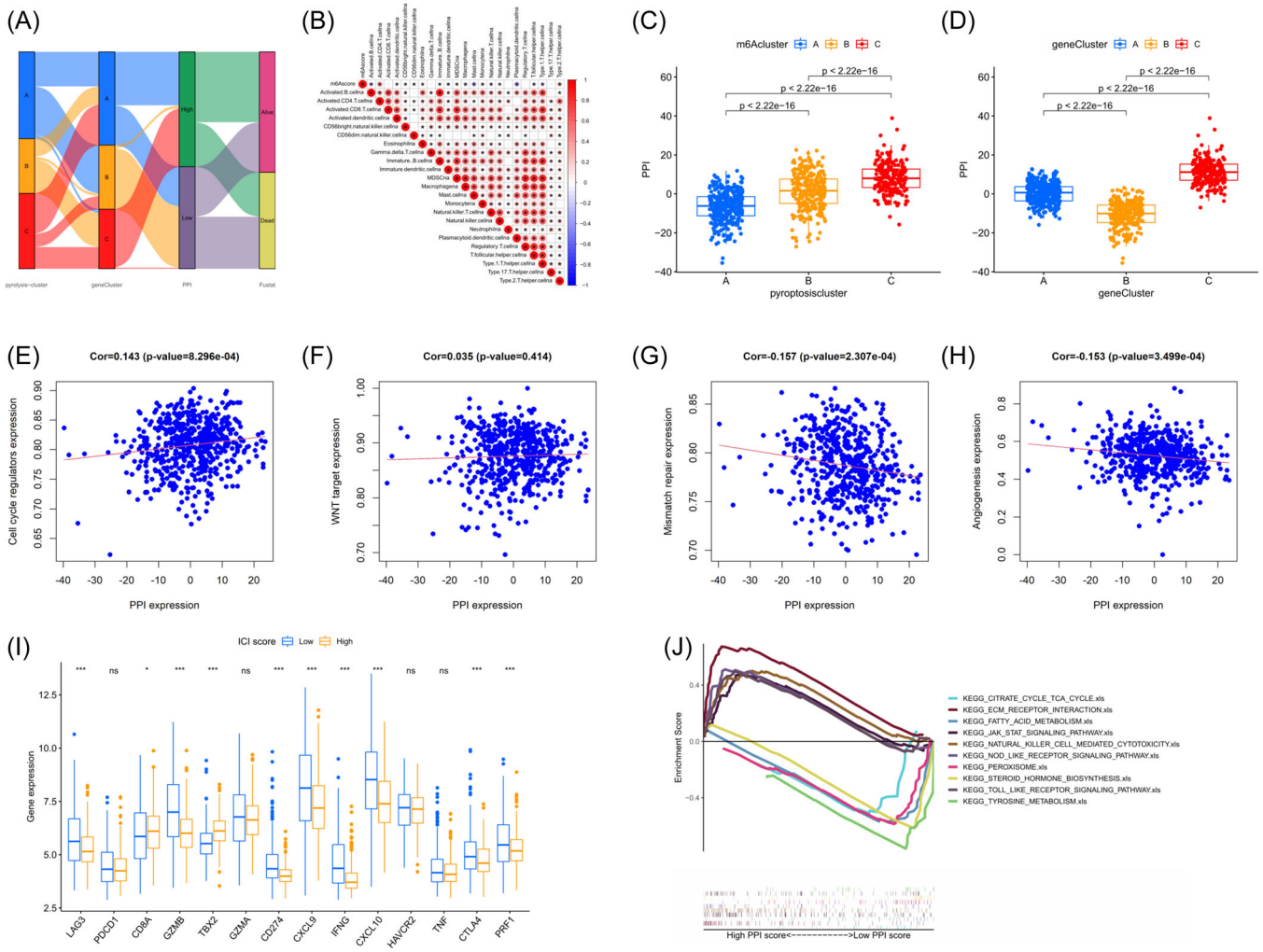

FIGURE 6 Establishment of the pyroptotic potential index (PPI) score model and exploration of the relevance of the immune features. (A) Alluvial diagram of pyroptosis clusters in groups with survival status, pyroptosis-gene cluster, and PPI score. (B) Correlations between the PPI score and known immune signatures in the meta-GEO cohort using Spearman's correlation analysis. (C) Differences in the PPI score among the three pyroptosis modification patterns in the meta-GEO cohort. The Kruskal–Wallis test was used to compare the statistical difference between the three gene clusters ($p < 0.001$). (D) Differences in the PPI score among the three gene clusters in the meta-GEO cohort ($p < 0.001$, Kruskal–Wallis test). (E–H) The scatter plot showed that PPI scores were significantly positively correlated with cell cycle regulators (E) and the WNT pathway (F), but negatively correlated with mismatch repair (G) and angiogenesis (H). (I) Immune-checkpoint-relevant genes (IDO1, CD274, HAVCR2, PDCD1, CTLA4, and LAG3) and immune-activation-relevant genes (CD8A, CXCL10, CXCL9, GZM A, GZMB, PRF1, IFNG, TBX2, and TNF) were expressed between the high and low PPI groups. (J) Gene set enrichment analysis (GSEA) was conducted to evaluate the difference between the high and low PPI groups.

scores. Figure 10B showed that temsirolimus, camptothecin, pazopanib, parthenolide, and docetaxel exhibited significant promise in treating HNSC ($p < 0.05$). Specifically, camptothecin and docetaxel have been extensively utilized as primary chemotherapy in clinical settings.

4 | DISCUSSION

Pyroptosis, alternatively referred to as cellular inflammatory necrosis, is initiated by the destruction of cell membranes resulting from the functioning of the majority of CASP family genes.[46] Cells undergoing pyroptosis display cellular enlargement and multiple bubble-shaped protrusions. The activation of CASP-1/4/5/11 is necessary for its dependency. The GSDMD-N protein creates minuscule openings measuring 1.1–2.4 nm across the cellular membrane.[47] Pyroptosis, serving as a type of programmed cellular demise, functions as the principal mechanism against infections. In addition, pyroptosis has demonstrated significant involvement in the development of tumors.[48,49] Pyroptosis, a process linked to tumorigenesis, invasion, and metastasis, involves the presence of inflamed vesicles, gastrin, and proinflammatory cytokines as crucial elements. Furthermore, pyroptosis significantly contributes to the innate immune response against intracellular pathogens and is also implicated in the

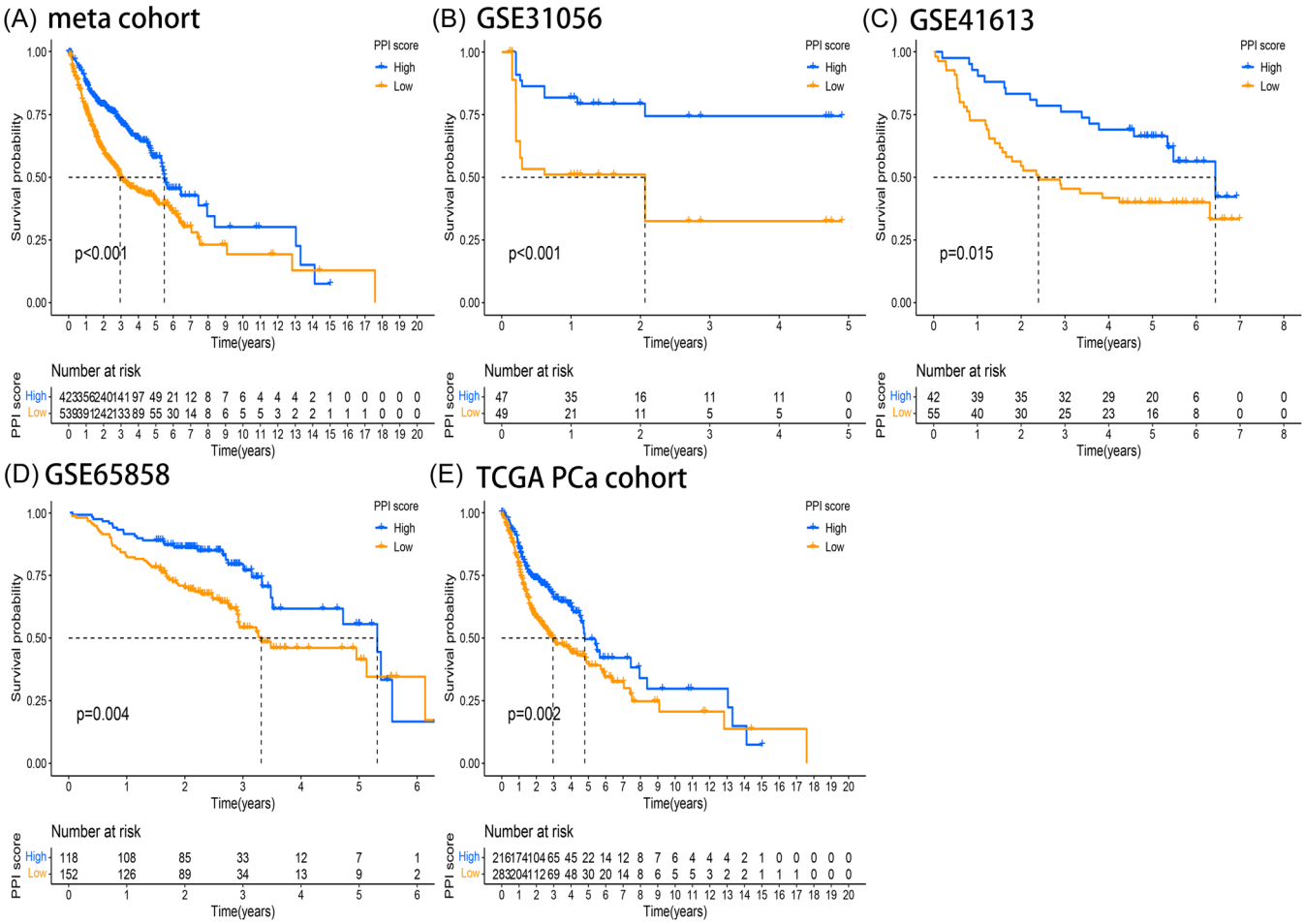

FIGURE 7 Kaplan–Meier survival curves of the high and low PPI groups. (A) GEO meta-cohort; (B) GSE31056; (C) GSE41613; (D) GSE65858; (E) TCGA HNSC cohort.

development of fatal infectious shock. Although cellular scorch death plays an important role in tumor development and antitumor processes, its specific role in HNSC has not been adequately explored. Consequently, we carried out a comprehensive investigation to assess the levels of gene expression associated with scorch death in both normal and HNSC tissues. In addition, the predictive significance of these genes was investigated, along with examining the association between scorch-induced mortality and the immune microenvironment of the tumor.

Initially, the expression levels of 33 presently recognized PRGs in HNSC and normal tissues were assessed, revealing significant differential expression in the majority of them. A meta-study was then conducted to analyze 1341 HNSC samples. The specimens were categorized into three separate subcategories, distinguished by varying immune characteristics, that were associated with diverse antitumor immune responses. An immune-inflamed phenotype was observed in Pyroptosis-C1, which was identified by the presence of immune activation and infiltration of tumor-infiltrating lymphocytes. An immune-excluded phenotype was observed in Pyroptosis-C2, which was identified by the existence of immune cells and stroma, along with the activation of EMT, TGF-β, and Wnt signaling pathways. The immune-desert phenotype was associated with an immunosuppressive TME in Pyroptosis-C3.

In the meantime, we conducted a thorough examination of the PRGs' expression and devised a technique for measuring the PPI index in HNSC. The results indicate that the PPI score serves as a reliable prognostic biomarker and predictor in evaluating the response to immunotherapy. The alteration of pyroptosis in the TME of HNSC has been documented to enhance immune suppression, which is linked to the survival and advancement of tumors.[50] Nevertheless, it is important to take into account molecular subcategories when implementing pyroptosis regulation as a therapeutic approach. We hypothesized that patients with a high PPI score may experience a favorable prognosis due to the presence of an antitumor immune response, suggesting potential benefits from immunotherapy. A negative outcome was linked to the immune-cold characteristic in the group with a low PPI score. Our previous findings are consistent with the high sensitivity of immunotherapy to high PPI scores, as predicted by TIDE and submap. While the precise manner in which pyroptosis controls the growth and proliferation of tumor cells is still unknown, the correlation we witnessed between PPI and key

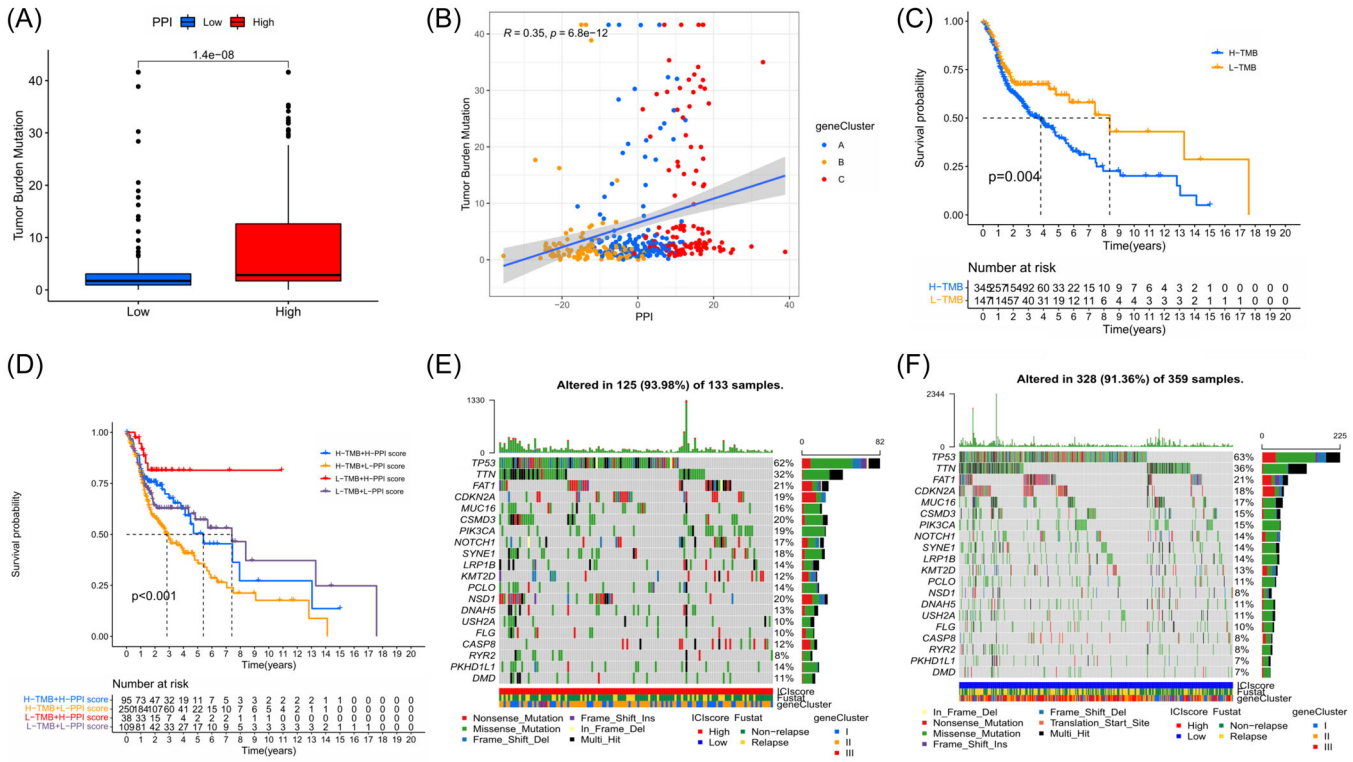

FIGURE 8 Correlation between PPI scores and somatic mutation. (A) The difference in tumor mutation burden (TMB) between the high and low PPI score groups (Wilcoxon test, $p = 0.0071$). (B) Scatter plots showed a positive correlation between the PPI scores and the mutation load in the meta-GEO cohort. There was a correlation between the PPI score and mutation load ($p = 0.00017$). (C) The Kaplan–Meier curve of the high and low TMB groups in the meta-GEO cohort (log rank test, $p < 0.05$). (D) The Kaplan–Meier curve of patients in the meta-GEO cohort stratified by TMB and PPI scores (log rank test, $p < 0.05$). (E, F) The oncoPrint was built using a high PPI score on the left (E) and a low ICI score on the right (F). Each column represents a patient.

TABLE 2 Relationship between PPI score and somatic variation.

Gene	H-wild	H-mutation	L-wild	L-mutation	*p* Value
NSD1	106 (79.7%)	27 (20.3%)	331 (92.2%)	28 (7.8%)	0.000179
PTPRZ1	125 (93.98%)	8 (6.02%)	354 (98.61%)	5 (1.39%)	0.011649
GRM1	122 (91.73%)	11 (8.27%)	349 (97.21%)	10 (2.79%)	0.015432
ELMO1	126 (94.74%)	7 (5.26%)	355 (98.89%)	4 (1.11%)	0.015467
FLNA	123 (92.48%)	10 (7.52%)	350 (97.49%)	9 (2.51%)	0.021506
VPS13C	122 (91.73%)	11 (8.27%)	348 (96.94%)	11 (3.06%)	0.025343
CUX2	126 (94.74%)	7 (5.26%)	354 (98.61%)	5 (1.39%)	0.032137
PKD1L1	126 (94.74%)	7 (5.26%)	354 (98.61%)	5 (1.39%)	0.032137
PCDHA6	126 (94.74%)	7 (5.26%)	354 (98.61%)	5 (1.39%)	0.032137
ASXL3	131 (98.5%)	2 (1.5%)	334 (93.04%)	25 (6.96%)	0.032441
PKHD1L1	115 (86.47%)	18 (13.53%)	334 (93.04%)	25 (6.96%)	0.034684
ERICH3	123 (92.48%)	10 (7.52%)	349 (97.21%)	10 (2.79%)	0.035363
GRIN2A	123 (92.48%)	10 (7.52%)	349 (97.21%)	10 (2.79%)	0.035363
FAT4	120 (90.23%)	13 (9.77%)	343 (95.54%)	16 (4.46%)	0.044565
EPHA2	132 (99.25%)	1 (0.75%)	340 (94.71%)	19 (5.29%)	0.044637

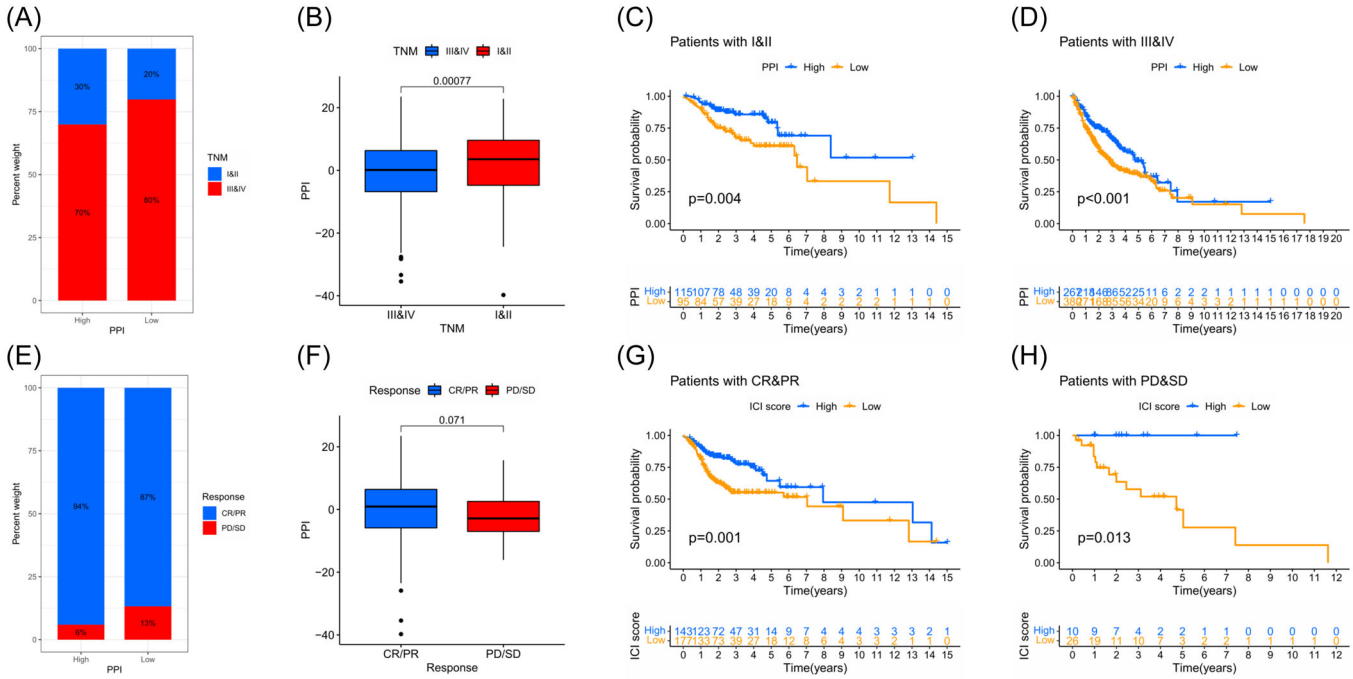

FIGURE 9 PPI scores correlated with clinical features. (A, B) PPI scores in groups with different pathological TNM stages (Wilcoxon test, $p < 0.0001$). (C, D) Stratified survival analysis showed that PPI scores were associated with survival. Kaplan–Meier curves for patients with high and low PPI scores and different TNM stages in the meta-GEO cohort (log rank test, $p < 0.05$). (E, F) PPI scores in groups with a different clinical response status (Wilcoxon test, $p < 0.0001$). (G, H) Stratified survival analysis showed that PPI scores were associated with survival. Kaplan–Meier curves for patients with high and low PPI scores and different clinical response statuses in the meta-GEO cohort (log rank test, $p < 0.05$).

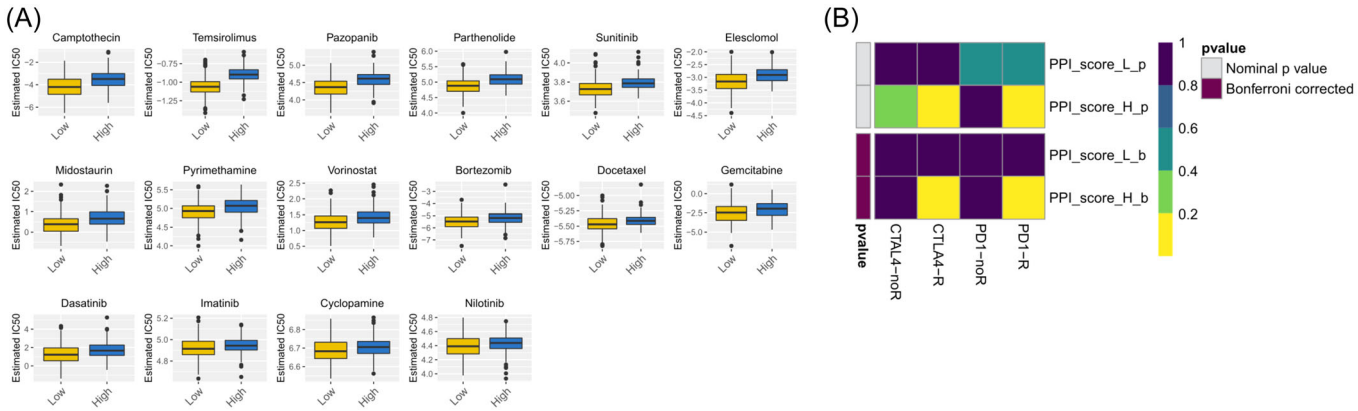

FIGURE 10 Role of PPI scores in predicting the benefit of immunotherapy. (A) Differential putative chemotherapeutic and immunotherapeutic response. The box plots of the estimated maximum inhibitory concentrations (IC50) for chemotherapeutic drugs are shown for high and low PPI score subsets. (B) Submap analysis showed that a high PPI score could be more sensitive to immunotherapy (Bonferroni-corrected $p < 0.05$).

characteristics of cancer has the potential to enhance our comprehension of the function of pyroptosis. In the majority of cancers, GSEA analysis revealed a strong correlation between the extent of pyroptosis and tumor-associated characteristics. In cancer, pyroptosis genes can have both oncogenic and tumor-suppressive functions, while protein–protein interaction serves as a safeguarding element in HNSC. Hence, the integration of the PPI subgroup and immune-related gene expression profiles may offer a new strategy for creating personalized treatment plans tailored to each patient.

To summarize, the results of this research not only enhanced our understanding of the process involved in pyroptosis in the HNSC TME but also introduced a new possible prognostic biomarker, the PPI score, to assist in precision immunotherapy.

TABLE 3 Screening of effective chemotherapeutic drugs for PPI grouping through GDSC database.

Drug	*p* Value
CEP.701	5.71E−42
Temsirolimus	3.14E−39
NU.7441	1.28E−38
AZD.2281	3.90E−32
WO2009093972	6.70E−29
GSK269962A	6.09E−27
Axitinib	3.60E−24
AZ628	1.57E−22
BX.795	3.44E−21
AZD7762	8.60E−21
Pazopanib	2.01E−20
AZD8055	4.31E−20
TW.37	6.08E−19
Parthenolide	7.90E−19
IPA.3	1.06E−18
Cytarabine	1.04E−17
GDC.0449	1.59E−16
PLX4720	4.32E−16
VX.702	4.90E−16
PD.173074	5.16E−15
NVP.BEZ235	1.61E−14
Camptothecin	1.75E−13
Sunitinib	2.01E−13
AP.24534	2.51E−13
Elesclomol	6.55E−13
NVP.TAE684	7.17E−12
JNJ.26854165	1.26E−11
AG.014699	2.96E−11
DMOG	5.73E−11
Midostaurin	8.20E−11
Pyrimethamine	4.23E−10
LFM.A13	2.50E−09
AZD6482	5.36E−09
Vorinostat	1.17E−08
ABT.888	1.99E−08
CGP.60474	2.71E−08
Bortezomib	1.09E−07
Docetaxel	2.20E−07
SB.216763	2.86E−07
PAC.1	3.07E−07
AMG.706	3.26E−07
BMS.754807	1.39E−06
OSI.906	1.69E−06
Gemcitabine	1.74E−06
JNK.Inhibitor.VIII	1.79E−06
CHIR.99021	1.80E−06
Dasatinib	3.92E−06
WH.4.023	8.50E−06
MS.275	3.96E−05
ZM.447439	4.32E−05
XMD8.85	0.000107
Imatinib	0.00011
BI.D1870	0.000121
BMS.509744	0.000199
Z.LLNle.CHO	0.000209
CMK	0.000213
PF.02341066	0.000248
GDC0941	0.00041
Cyclopamine	0.000563
BAY.61.3606	0.001202
Nilotinib	0.001397
AS601245	0.001475
KU.55933	0.002407
SL.0101.1	0.002917
Vinblastine	0.003376
PHA.665752	0.003836
SB590885	0.004598
Bexarotene	0.004692
Cisplatin	0.011966
A.770041	0.016861
RO.3306	0.017973
X681640	0.021013
Methotrexate	0.024357
Obatoclax.Mesylate	0.029282

AUTHOR CONTRIBUTIONS

Yan Long: Supervision; visualization; writing—original draft. **Yadong Wu**: Conceptualization; software; supervision. **Juxiang Peng**: Conceptualization; investigation; methodology. **Jukun Song**: Conceptualization; supervision; writing—original draft; writing—review and editing. **Na Li**: Visualization; writing—review and editing.

ACKNOWLEDGMENTS

The work was supported by the Guizhou Provincial People's Hospital Youth Fund GZSYQN[2016]09.

CONFLICT OF INTEREST STATEMENT

The authors declare that they have no competing interests.

DATA AVAILABILITY STATEMENT

Data availability could be obtained from TCGA and GEO websites.

ORCID

Jukun Song http://orcid.org/0000-0003-2542-9340

REFERENCES

1. Zhong F, Lu HP, Chen G, et al. The clinical significance of apolipoprotein L1 in head and neck squamous cell carcinoma. *Oncol Lett*. 2020;20(6):377.
2. Huang C, Cintra M, Brennan K, et al. Development and validation of radiomic signatures of head and neck squamous cell carcinoma molecular features and subtypes. *EBioMedicine*. 2019;45:70-80.
3. Siegel RL, Miller KD, Fuchs HE, Jemal A. Cancer statistics, 2021. *CA Cancer J Clin*. 2021;71(1):7-33.
4. Marur S, Forastiere AA. Head and neck squamous cell carcinoma: update on epidemiology, diagnosis, and treatment. *Mayo Clin Proc*. 2016;91(3):386-396.
5. Singh A, Mishra A, Singhvi H, et al. Optimum surgical margins in squamous cell carcinoma of the oral tongue: is the current definition adequate? *Oral Oncol*. 2020;111:104938.
6. Chan GG, Tai BC, Liang S, Lim DT, Soo KC. Squamous cell carcinoma of the head and neck (HNSCC)--multi-modality treatment and impact on survival. *Asian J Surg*. 2002;25(1):35-40.
7. Jain P. Pyroptosis and oral cancer. *J Contemp Dent Pract*. 2019;20(9):1001-1002.
8. Bullon P, Pavillard LE, de la Torre-Torres R. Inflammasome and oral diseases. *Exp Suppl*. 2018;108:153-176.
9. Muñoz-Arias I, Doitsh G, Yang Z, Sowinski S, Ruelas D, Greene WC. Blood-derived CD4 T cells naturally resist pyroptosis during abortive HIV-1 infection. *Cell Host Microbe*. 2015;18(4):463-470.
10. Wu DD, Pan PH, Liu B, et al. Inhibition of alveolar macrophage pyroptosis reduces lipopolysaccharide-induced acute lung injury in mice. *Chin Med J*. 2015;128(19):2638-2645.
11. Geng Y, Ma Q, Liu YN, et al. Heatstroke induces liver injury via IL-1β and HMGB1-induced pyroptosis. *J Hepatol*. 2015;63(3):622-633.
12. Tan MS, Tan L, Jiang T, et al. Amyloid-β induces NLRP1-dependent neuronal pyroptosis in models of Alzheimer's disease. *Cell Death Dis*. 2014;5:e1382.
13. Guo J, Zheng J, Mu M, et al. GW4064 enhances the chemosensitivity of colorectal cancer to oxaliplatin by inducing pyroptosis. *Biochem Biophys Res Commun*. 2021;548:60-66.
14. Deng BB, Jiao BP, Liu YJ, Li YR, Wang GJ. BIX-01294 enhanced chemotherapy effect in gastric cancer by inducing GSDME-mediated pyroptosis. *Cell Biol Int*. 2020;44(9):1890-1899.
15. Fountzilas E, Kotoula V, Angouridakis N, et al. Identification and validation of a multigene predictor of recurrence in primary laryngeal cancer. *PLoS One*. 2013;8(8):e70429.
16. Reis PP, Waldron L, Perez-Ordonez B, et al. A gene signature in histologically normal surgical margins is predictive of oral carcinoma recurrence. *BMC Cancer*. 2011;11:437.
17. Chen C, Méndez E, Houck J, et al. Gene expression profiling identifies genes predictive of oral squamous cell carcinoma. *Cancer Epidemiol Biomarkers Prevent*. 2008;17(8):2152-2162.
18. Walter V, Yin X, Wilkerson MD, et al. Molecular subtypes in head and neck cancer exhibit distinct patterns of chromosomal gain and loss of canonical cancer genes. *PLoS One*. 2013;8(2):e56823.
19. Lohavanichbutr P, Méndez E, Holsinger FC, et al. A 13-gene signature prognostic of HPV-negative OSCC: discovery and external validation. *Clin Cancer Res*. 2013;19(5):1197-1203.
20. Wichmann G, Rosolowski M, Krohn K, et al. The role of HPV RNA transcription, immune response-related gene expression and disruptive TP53 mutations in diagnostic and prognostic profiling of head and neck cancer. *Int J Cancer*. 2015;137(12):2846-2857.
21. Davis S, Meltzer PS. GEOquery: a bridge between the Gene Expression Omnibus (GEO) and BioConductor. *Bioinformatics*. 2007;23(14):1846-1847.
22. Johnson WE, Li C, Rabinovic A. Adjusting batch effects in microarray expression data using empirical Bayes methods. *Biostatistics*. 2007;8(1):118-127.
23. Hellmann MD, Ciuleanu TE, Pluzanski A, et al. Nivolumab plus ipilimumab in lung cancer with a high tumor mutational burden. *N Engl J Med*. 2018;378(22):2093-2104.
24. Wilkerson MD, Hayes DN. ConsensusClusterPlus: a class discovery tool with confidence assessments and item tracking. *Bioinformatics*. 2010;26(12):1572-1573.
25. Hänzelmann S, Castelo R, Guinney J. GSVA: gene set variation analysis for microarray and RNA-seq data. *BMC Bioinformatics*. 2013;14:7.
26. Yu G, Wang LG, Han Y, He QY. clusterProfiler: an R package for comparing biological themes among gene clusters. *OMICS*. 2012;16(5):284-287.
27. Barbie DA, Tamayo P, Boehm JS, et al. Systematic RNA interference reveals that oncogenic KRAS-driven cancers require TBK1. *Nature*. 2009;462(7269):108-112.
28. Charoentong P, Finotello F, Angelova M, et al. Pan-cancer immunogenomic analyses reveal genotype-immunophenotype relationships and predictors of response to checkpoint blockade. *Cell Rep*. 2017;18(1):248-262.
29. Ritchie ME, Phipson B, Wu D, et al. limma powers differential expression analyses for RNA-sequencing and microarray studies. *Nucleic Acids Res*. 2015;43(7):e47.
30. Zeng D, Li M, Zhou R, et al. Tumor microenvironment characterization in gastric cancer identifies prognostic and immunotherapeutically relevant gene signatures. *Cancer Immunol Res*. 2019;7(5):737-750.
31. Sotiriou C, Wirapati P, Loi S, et al. Gene expression profiling in breast cancer: understanding the molecular basis of histologic grade to improve prognosis. *J Natl Cancer Inst*. 2006;98(4):262-272.
32. Mayakonda A, Lin DC, Assenov Y, Plass C, Koeffler HP. Maftools: efficient and comprehensive analysis of somatic variants in cancer. *Genome Res*. 2018;28(11):1747-1756.
33. Pérez-García JM, Llombart-Cussac A, Gion M, et al. Pembrolizumab plus eribulin in hormone-receptor-positive, HER2-negative, locally recurrent or metastatic breast cancer (KELLY): an open-label, multicentre, single-arm, phase trial. *Eur J Cancer*. 2021;148:382-394.
34. Curran MA, Montalvo W, Yagita H, Allison JP. PD-1 and CTLA-4 combination blockade expands infiltrating T cells and reduces regulatory T and myeloid cells within B16 melanoma tumors. *Proc Natl Acad Sci U S A*. 2010;107(9):4275-4280.

35. Mariathasan S, Turley SJ, Nickles D, et al. TGFβ attenuates tumour response to PD-L1 blockade by contributing to exclusion of T cells. *Nature*. 2018;554(7693):544-548.
36. Hugo W, Zaretsky JM, Sun L, et al. Genomic and transcriptomic features of response to Anti-PD-1 therapy in metastatic melanoma. *Cell*. 2017;168(3):542.
37. Jiang P, Gu S, Pan D, et al. Signatures of T cell dysfunction and exclusion predict cancer immunotherapy response. *Nature Med*. 2018;24(10):1550-1558.
38. Hoshida Y, Brunet JP, Tamayo P, Golub TR, Mesirov JP. Subclass mapping: identifying common subtypes in independent disease data sets. *PLoS One*. 2007;2(11):e1195.
39. Yang W, Soares J, Greninger P, et al. Genomics of drug sensitivity in cancer (GDSC): a resource for therapeutic biomarker discovery in cancer cells. *Nucleic Acids Res*. 2013;41:955-961.
40. Geeleher P, Cox NJ, Huang RS. Clinical drug response can be predicted using baseline gene expression levels and in vitro drug sensitivity in cell lines. *Genome Biol*. 2014;15(3):R47.
41. Seiwert TY, Burtness B, Mehra R, et al. Safety and clinical activity of pembrolizumab for treatment of recurrent or metastatic squamous cell carcinoma of the head and neck (KEYNOTE-012): an open-label, multicentre, phase 1b trial. *Lancet Oncol*. 2016;17(7):956-965.
42. Cristescu R, Mogg R, Ayers M, et al. Pan-tumor genomic biomarkers for PD-1 checkpoint blockade-based immunotherapy. *Science*. 2018;362(6411):eaar3593.
43. Danaher P, Warren S, Lu R, et al. Pan-cancer adaptive immune resistance as defined by the Tumor Inflammation Signature (TIS): results from The Cancer Genome Atlas (TCGA). *J Immunother Cancer*. 2018;6(1):63.
44. Hatakeyama K, Nagashima T, Ohshima K, et al. Mutational burden and signatures in 4000 Japanese cancers provide insights into tumorigenesis and response to therapy. *Cancer Sci*. 2019;110(8):2620-2628.
45. McGray AJR, Huang RY, Battaglia S, et al. Oncolytic Maraba virus armed with tumor antigen boosts vaccine priming and reveals diverse therapeutic response patterns when combined with checkpoint blockade in ovarian cancer. *J Immunother Cancer*. 2019;7(1):189.
46. Paldino E, D'Angelo V, Laurenti D, Angeloni C, Sancesario G, Fusco FR. Modulation of inflammasome and pyroptosis by olaparib, a PARP-1 inhibitor, in the R6/2 mouse model of Huntington's disease. *Cells*. 2020;9(10):2286.
47. de Torre-Minguela C, Gomez AI, Couillin I, Pelegrin P. Gasdermins mediate cellular release of mitochondrial DNA during pyroptosis and apoptosis. *FASEB J*. 2021;35(8):e21757.
48. Moujalled D, Strasser A, Liddell JR. Molecular mechanisms of cell death in neurological diseases. *Cell Death Differ*. 2021;28(7):2029-2044.
49. Lou J, Zhou Y, Feng Z, et al. Caspase-independent regulated necrosis pathways as potential targets in cancer management. *Front Oncol*. 2020;10:616952.
50. Croker BA, O'Donnell JA, Gerlic M. Pyroptotic death storms and cytopenia. *Curr Opin Immunol*. 2014;26:128-137.

SUPPORTING INFORMATION

Additional supporting information can be found online in the Supporting Information section at the end of this article.

How to cite this article: Long Y, Wu Y, Peng J, Song J, Li N. Pyroptosis-related gene signatures are associated with prognosis and tumor microenvironment infiltration in head and neck cancer. *Health Sci Rep*. 2023;6:e1622. doi:10.1002/hsr2.1622